

A HYDRODYNAMIC MODEL OF
MICROMETEOROID IMPACT

By

BENARD A. SODEK, JR.

Bachelor of Science
Loyola University of the South
New Orleans, Louisiana
1959

Master of Science
Oklahoma State University
Stillwater, Oklahoma
1965

Submitted to the Faculty of the Graduate
School of the Oklahoma State
University in partial fulfillment of the
requirements for the degree of
DOCTOR OF PHILOSOPHY
May 22, 1966

A HYDRODYNAMIC MODEL OF
MICROMETEOROID IMPACT

Thesis approved:

Francis C. Judd

Thesis Advisor

Leon W. Schroeder

W. Lewis

H. Harrington

F. Wayne Johnson

J. H. Briggs

Dean of the Graduate School

621823

PREFACE

This problem was started at the suggestion of Dr. F. C. Todd who acted as my adviser and project supervisor. I am indebted to him for his guidance, assistance, patience, and encouragement during the progress of this work.

The purpose of this research is to investigate a plausible mechanism of hypervelocity impact. The incidence of a 10^{-9} gram aluminum microparticle on a semi-infinite aluminum target is described in terms of fluid flow in two space dimensions.

Computer time for the actual production of the solution was made available by Mr. W. Merle Alexander of Goddard Space Flight Center. I have special thanks for Mr. William Cahill and his staff of this installation who greatly facilitated scheduling of computer time during my visits and who supervised the exchange by mail of further computer programs.

The work was carried out under NASA Contract number NASr-7 administered through the Research Foundation of Oklahoma State University.

TABLE OF CONTENTS

Chapter	Page
I. INTRODUCTION AND SURVEY OF THE PROBLEM	1
Proposed Impact Theories	2
Statement of the Problem	4
II. FUNDAMENTALS OF THE INVISCID FLUID MODEL	8
The Equations of Fluid Flow	8
A Brief Description of Shock Waves	12
The Introduction of Dissipation	17
The High Pressure Equation of State	20
Dimensionless Differential Equations	21
III. THE NUMERICAL METHOD	24
The Two Dimensional Equations	24
Finite Difference Mesh Configuration and Cycling	29
Quality of Solutions	33
Development of Computer Program	36
IV. DEVELOPMENT AND PRESENTATION OF SOLUTIONS	40
Initial Values	41
Boundary Conditions	43
The Solutions	44
Organization of Solutions	44
Shock Wave Formation and Decay	45
Pressure Profiles	46
Two Dimensional Distributions	51
Pressure and Material Velocity Distributions	53
Density Distributions	63
Internal Energy Distributions	67
Cavity Formation	71
Dissipation of the Peak Pressure	75
Discussion of Results	77
V. SUMMARY AND SUGGESTIONS FOR FUTURE WORK	78
BIBLIOGRAPHY	80

LIST OF FIGURES

Figure	Page
1. Plane Shock Front	15
2. Typical Pressure Profile of a One Dimensional Shock Wave	17
3. Cell Boundary Notation	27
4. Initial Partial Area Calculation	31
5. Computer Flow Diagram	39
6. Initial Value Illustration	42
7. Pressure Profiles Along Normal Axis (Time = $.0524 \times 10^{-9}$, $.105 \times 10^{-9}$, $.224 \times 10^{-9}$ seconds)	47
8. Pressure Profiles Along Normal Axis (Time = $.371 \times 10^{-9}$, $.517 \times 10^{-9}$ seconds)	48
9. Pressure Profiles Along Normal Axis (Time = $.664 \times 10^{-9}$, $.884 \times 10^{-9}$ seconds)	49
10. Pressure Contours and Velocity Distributions (Time = $.0384 \times 10^{-9}$, $.105 \times 10^{-9}$ seconds)	54
11. Pressure Contours and Velocity Distribution (Time = $.172 \times 10^{-9}$ seconds)	55
12. Pressure Contours and Velocity Distribution (Time = $.371 \times 10^{-9}$ seconds)	56
13. Pressure Contours and Velocity Distribution (Time = $.517 \times 10^{-9}$ seconds)	57
14. Pressure Contours and Velocity Distribution (Time = $.811 \times 10^{-9}$ seconds)	58
15. Pressure Contours and Velocity Distribution (Time = 1.23×10^{-9} seconds)	59

16.	Constant Density Contours (Time = $.0384 \times 10^{-9}$, $.172 \times 10^{-9}$ seconds)	64
17.	Constant Density Contours (Time = $.517 \times 10^{-9}$ seconds)	65
18.	Constant Density Contours (Time = 1.23×10^{-9} seconds)	66
19.	Constant Energy Contours (Time = $.105 \times 10^{-9}$ seconds)	68
20.	Constant Energy Contours (Time = $.371 \times 10^{-9}$ seconds)	69
21.	Constant Energy Contours (Time = $.811 \times 10^{-9}$ seconds)	70
22.	Position of Surface at Various Times (Time = $.0384 \times 10^{-9}$, $.105 \times 10^{-9}$, $.172 \times 10^{-9}$, $.371 \times 10^{-9}$ seconds)	72
23.	Position of Surface at Various Times (Time = $.371 \times 10^{-9}$, $.517 \times 10^{-9}$, $.811 \times 10^{-9}$, 1.23×10^{-9} seconds)	73
24.	Peak Shock Pressure as a Function of Maximum Shock Penetration.	76

CHAPTER I

INTRODUCTION

Micrometeoroids are defined as particles which have a mass of less than 10^{-4} grams and velocities that range from 30,000 to 240,000 feet per second. When these microparticles are smaller than 10^{-11} to 10^{-12} grams, the pressure of the radiation from the Sun will eventually push these particles outside the orbit of the earth. (1). They are detected by devices placed on space vehicles. One device that has been successfully used is a photomultiplier tube with a vapor deposited aluminum film covering the face. (2). The micrometeoroids impinging upon the face of the photomultiplier are known to produce a pulse of current through the tube.

The NASA project for which this thesis is a contribution was initiated as an analytical and limited experimental study of micrometeoroid impact on the coated photomultiplier. The project is concerned with the mechanics of impact which result in producing light to activate the photomultiplier tube and which result in producing the craters associated with hypervelocity impacts.

Proposed Impact Theories

A few published articles have reported methods to predict and analyze the impact phenomena of small particles with hypervelocities. The latter term includes all velocities in excess of the velocity of sound in the target. One article approaches the problem from the thermal damage theory. (3). In this theory, the flash of light accompanying the impact is attributed to incandescence of the target and of the micro-particle in the immediate vicinity of the impact. In this concept, the crater is caused by vaporization and explosion of some of the target. This model has been criticized for the following reasons. The crater is found to be lined with projectile material. The thermal model, however, offers no explanation for this lining effect. Conversely, it would appear that as the target material is converted to a vapor. The succeeding explosion should, therefore, hurl both surrounding target material and the projectile out of the crater. Another reason for not accepting the entire thermal damage model has been suggested by calculations based on a limited amount of experimental evidence. (4). It was found that over 50 percent of the kinetic energy is required to heat and melt the volume of target material that is removed from the crater. This leaves very little energy for evaporation and radiation processes.

Bjork (5) examined the problem of a high-velocity projectile of cylindrical symmetry impinging upon a semi-infinite solid. Bjork used a hydrodynamic model of impact which suggests that the penetration of a projectile into the target is much the same as one fluid penetrating another. That is, the target and projectile, under the tremendous forces of impact, both become fluid. The hemispherical shape of the crater is attributed to a strong radial shock wave that is initiated at the point of impact. One defect of this model is that it does not include a mechanism for the production of light. This thesis shares a number of assumptions and procedures with the work of Bjork.

A different theory of impact has been proposed by F. C. Todd (6), project supervisor. This theory proposes that a plasma is formed by the strong radial shock from the impact. A plasma is defined as a mixture of ions and electrons. It will start to form from the application of pressure alone at a pressure of approximately 100,000 atmospheres. (7). The radiation that accompanies the impact results from the electrons in the plasma recombining to form neutral atoms. It is also proposed that a radial shock wave would account for the nearly hemispherical shape of the crater. The proposed plasma model partially agrees with the assumption made in both the thermal damage and hydrodynamic models of impact. The plasma model includes a radial shock which was assumed to accompany the hydrodynamic model and it also assumes that the

material in the immediate vicinity of the impact regions has a high energy density as does the thermal model. It differs from the thermal damage model in that for thermal damage, the high energy density is in the form of a high temperature; while, for the plasma model, more of the energy is in the form of recoverable potential energy.

Statement of the Problem

The subject of this thesis is the investigation of the hydrodynamic mechanism involved in the plasma theory proposed by F. C. Todd. It is particularly desired to determine whether it is possible to theoretically calculate the formation and propagation of a shock wave resulting from a hypervelocity impact.

When a microparticle, traveling at hypersonic velocities, strikes a target, a crater is formed which is many times larger than the projectile and is centered about the point of initial contact. The crater may have a small lip around its edge. Rapid sequence photographs show that a fine spray of material is ejected from the boundaries of the crater as it forms. This evidence is to be contrasted with the more familiar impact of subsonic projectiles. These leave long, deep holes in the target which are only slightly larger than the projectile itself.

Reasons for assuming inviscid, hydrodynamic flow in a hypervelocity impact have been summarized by Charters(8).

His qualitative description of penetration shares a number of features with the quantitative results of this thesis. Much of the qualitative discussion that follows is based on photographs published by Charters. The observation that the formation of the crater requires many microseconds suggests a sustained disturbance, such as from a shock wave, in contrast to an explosive reaction. The material is ejected by hydrodynamic flow along the walls of the crater. From these comments and the symmetrical shape of the crater, the hydrodynamic model appears to provide the best clarification of the results.

A basic feature of the model to be investigated is the formation of two shock waves. One strong shock wave radiates out from the point of impact compressing and accelerating the material of the target. This shock wave precedes the penetrating microparticle into the target. The other shock wave propagates backward against the motion of the impacting microparticle. This shock wave eventually reaches the back edge of the microparticle and is reflected back into the direction of motion of the first shock.

The computer solution does not distinguish between the aluminum of the incident sphere and the aluminum of the semi-infinite target after they come into contact. The details of the impact are, consequently, a little difficult to follow and to interpret. Anticipating the general results of the solution, the impacting microparticle appears to

compress the target material ahead of and surrounding itself. This results in the hydrodynamic flow of the target material up, around the entering particle and out of the target. According to the pictures from Charters' article, this material leaves the target as spray.

The model to be studied involves the assumption of inviscid fluid behavior of the target and projectile, and it neglects heat conduction, radiation, and other forms of energy dissipation. It will develop that the proposed program requires a large computer memory. The inclusion of any of other corrections to the impact problem would require an extremely large increase in the length of time on the computer.

The problem for solution is the impact of a spherical, aluminum particle of mass 10^{-9} grams. The velocity of impact is 118,000 feet per second. The target is a semi-infinite block of aluminum.

The work presented in this thesis may be briefly outlined as follows:

- (1) The partial differential equations of large-scale fluid flow are presented and converted to a dimensionless form.
- (2) The dimensionless hydrodynamic equations are converted to difference equations for numerical solution.
- (3) The difference equations are programmed.

- (4) The computer program, using prescribed initial conditions and boundary conditions, gives solutions describing the initial stages of shock wave propagation and crater development.

CHAPTER II

FUNDAMENTALS OF THE INVISCID FLUID MODEL

When a microparticle with a velocity of 36 kilometers per second impacts on a target, the pressure is calculated to be millions of atmospheres. (4,5). At such extreme conditions, both projectile and target are considered to be fluids. The necessary mathematical formulas to describe inviscid flow exist, are well known, and are proven by experiment. They are the three equations for the conservation of mass, energy and momentum. Boundary conditions and equations of state for the materials of the microparticle and the target are required to describe conditions on each side of the impact. The entropy must also increase across the shock front. These equations do not have a closed solution or a practically useful approximate solution. The mathematics are generalized as far as possible and prepared for solution by numerical methods which utilize a high speed electronic computer.

The Equations of Fluid Flow

The basic equations of the hydrodynamic model are obtained from the application of conservation laws to

to a perfect fluid. There are two forms in which these equations can be tied to a physical region. The Eulerian reference frame deals with the values of dependent variables at fixed points in space and time. The Lagrangean system describes the motion of a fluid in terms of the trajectories of individual elements. In most cases and particularly for two and three dimensional cases, Euler's representation is preferable from a mathematical and a physical point of view, according to Courant and Friedrichs (8). The equations of conservation, in Eulerian coordinates take the following form:

$$\frac{D\rho}{Dt} + \rho \nabla \cdot \vec{v} = 0 \quad 2.1$$

$$\rho \frac{D\vec{v}}{Dt} + \nabla p = 0 \quad 2.2$$

$$\frac{DI}{Dt} - \frac{p}{\rho^2} \frac{D\rho}{Dt} = 0 \quad 2.3$$

where $\frac{D}{Dt} = \frac{\partial}{\partial t} + \vec{v} \cdot \nabla$. (17). The independent variables are the time t , and a set of spatial coordinates. The dependent variables are

ρ = density

\vec{v} = material velocity

p = pressure

I = specific internal energy

An auxiliary equation is necessary to relate the pressure, p , to other fluid variables.

$$p = p(\rho, I)$$

This is the equation of state which yields the pressure as a function of the density and the specific internal energy.

Previous solutions of large scale fluid motion in two dimensions have usually employed rectangular or cylindrical coordinates. An examination of experimental evidence and of earlier analytic approaches indicates that a radial, or polar, coordinate system is a better representation for this particular problem. The shapes of craters from high velocity impacts are virtually perfect hemispheres. This would indicate that the transfer of energy from projectile to target is largely accomplished by means of radial flow. This description complicates the representation of the impacting sphere, but the desire to portray the formation and propagation of the expected shock front is an overriding consideration. Since experimental evidence of the actions of target and projectile shows no azimuthal effects, symmetry of the solution about an axis normal to the semi-infinite target will be assumed.

According to Rae (24), the first conservation equation, in spherical polar coordinates, is

$$\begin{aligned} \frac{\partial \rho}{\partial t} + \frac{w}{r} \frac{\partial \rho}{\partial \theta} + \frac{\rho}{r} \frac{\partial w}{\partial \theta} + \frac{\rho w}{r} \frac{\partial \theta}{\partial \theta} + u \frac{\partial \rho}{\partial r} \\ + \rho \frac{\partial u}{\partial r} + 2 \frac{\rho u}{r} = 0 \end{aligned} \quad 2.5$$

where r and θ are spatial coordinates and u and w are the corresponding velocity components.

The equation of motion, 2.2, yields two equations.

$$\frac{\partial u}{\partial t} + u \frac{\partial u}{\partial r} + \frac{w}{r} \frac{\partial u}{\partial \theta} - \frac{w^2}{r} + \frac{1}{\rho} \frac{\partial p}{\partial r} = 0 \quad 2.6$$

$$\frac{\partial w}{\partial t} + u \frac{\partial w}{\partial r} + \frac{w}{r} \frac{\partial w}{\partial \theta} + \frac{uw}{r} + \frac{1}{\rho r} \frac{\partial p}{\partial \theta} = 0 \quad 2.7$$

The equation of conservation of energy is

$$\begin{aligned} \frac{\partial I}{\partial t} + u \frac{\partial I}{\partial r} + \frac{w}{r} \frac{\partial I}{\partial \theta} \\ - \frac{p}{\rho^2} \left(\frac{\partial p}{\partial t} + u \frac{\partial p}{\partial r} + \frac{w}{r} \frac{\partial p}{\partial \theta} \right) = 0 \end{aligned} \quad 2.8$$

The equation of continuity, 2.5, can be more compactly written as

$$\frac{\partial \rho}{\partial t} + \frac{\partial (r^2 \rho u)}{r^2 \partial r} + \frac{\partial (\sin \theta \rho w)}{r \sin \theta \partial \theta} \quad 2.9$$

Using this equation in 2.6 and 2.7, both equations can be put into a form more suitable for numerical solution.

$$\begin{aligned} \frac{\partial (\rho u)}{\partial t} + \frac{\partial (r^2 \rho u u)}{r^2 \partial r} + \frac{\partial (\sin \theta \rho w u)}{r \sin \theta \partial \theta} - \frac{\rho w^2}{r} \\ + \frac{\partial p}{\partial r} = 0 \end{aligned} \quad 2.10$$

$$\begin{aligned} \frac{\partial (\rho w)}{\partial t} + \frac{\rho u w}{r} + \frac{1}{r} \frac{\partial p}{\partial \theta} \\ + \frac{\partial (r^2 \rho u w)}{r^2 \partial r} + \frac{\partial (\sin \theta \rho w w)}{r \sin \theta \partial \theta} = 0 \end{aligned} \quad 2.11$$

A similar form can be obtained for equation 2.8 by using equations 2.9, 2.10, and 2.11.

$$\begin{aligned} \frac{d(\rho\psi)}{dt} + \frac{d(r^2\rho u\psi)}{r^2 dr} + \frac{d(\sin\theta\rho w\psi)}{r\sin\theta d\theta} \\ + \frac{d(r^2\rho u)}{r^2 dr} + \frac{d(\sin\theta\rho w)}{r\sin\theta d\theta} \end{aligned} \quad 2.12$$

where $\psi = I + \frac{1}{2}u^2 + \frac{1}{2}w^2$ is the total energy per unit mass.

Since the conservation of momentum requires two equations, the three conservation conditions require four equations, 2.9 to 2.11. Two more relations are required to solve for the propagation of a shock wave. These are an equation of state and the condition that the entropy increase across the shock front. An equation of state is represented in functional notation by equation 2.4. This relation will be discussed in more detail in a following section. Although the equation of state involves only three variables, auxiliary relations are needed to interrelate five unknowns the density, ρ ; the velocities, u and w ; the internal energy I ; and the pressure, p .

A Brief Description of Shock Waves

Shock waves are dilatational waves in a non-viscous fluid medium with a negligible resistance to shear. For this reason, the flow of highly compressed solids may be represented by the equations of hydrodynamic flow. In the

propagation of a shock front, the pressure rises to a high value in a very thin zone. This infinitesimal region of rapidly changing pressure, density, and internal energy appears as a discontinuity in the equations for hydrodynamic flow.

To obtain solutions, it is necessary to derive conditions that relate the state of the material on one side of the shock front to that on the other side. The conditions are usually called the Rankine - Hugoniot conditions.

Consider a plane shock front, as illustrated in Figure 1, traveling with a velocity of propagation Σ into stationary material at pressure p_0 , density ρ_0 , and specific internal energy e_0 . The encompassed material is accelerated to a particle velocity σ by the passage of the shock front and is compressed to a density $\rho > \rho_0$. The state of the shocked portion of the medium is related to the undisturbed state by a series of conservation equations:

Conservation of mass

$$\rho_0 \Sigma = \rho (\Sigma - \sigma)$$

Conservation of momentum

$$p - p_0 = \rho_0 \Sigma \sigma$$

Conservation of energy

$$\rho \sigma = \rho_0 \Sigma (e - e_0 + \sigma^2/2)$$

These give the Rankine-Hugoniot energy equation

$$e - e_0 = \frac{1}{2} (V_0 - V) (p + p_0)$$

where $V = 1/\rho$.

These equations involve five parameters of the shocked state. One more relation, an equation of state, is required before the specification of one variable is sufficient to permit the calculation of the other four. When the equation of state is given in the form $e = e(p, V)$, it may be combined with the Rankine - Hugoniot energy equation to yield a relation between the pressure and the specific volume. Such an expression is known as the "Hugoniot Curve" or simply as the "Hugoniot." This Hugoniot is unique for a given material, as are an isotherm or an adiabat. This special pressure volume curve represents the totality of the p, V points which may be reached by a shock transition from an initial state p_0, V_0 .

A typical pressure profile for an one dimensional shock wave is indicated in Figure 2. Ahead of the shock front the material is undisturbed. At the head of the wave the pressure, p increases almost instantaneously to its peak value and then decreases toward zero behind the shock front. This jump marks the position of the advancing shock wave the propagation velocity, Σ , of the shock front is supersonic with respect to the undisturbed material, that is

$$\Sigma > c_0$$

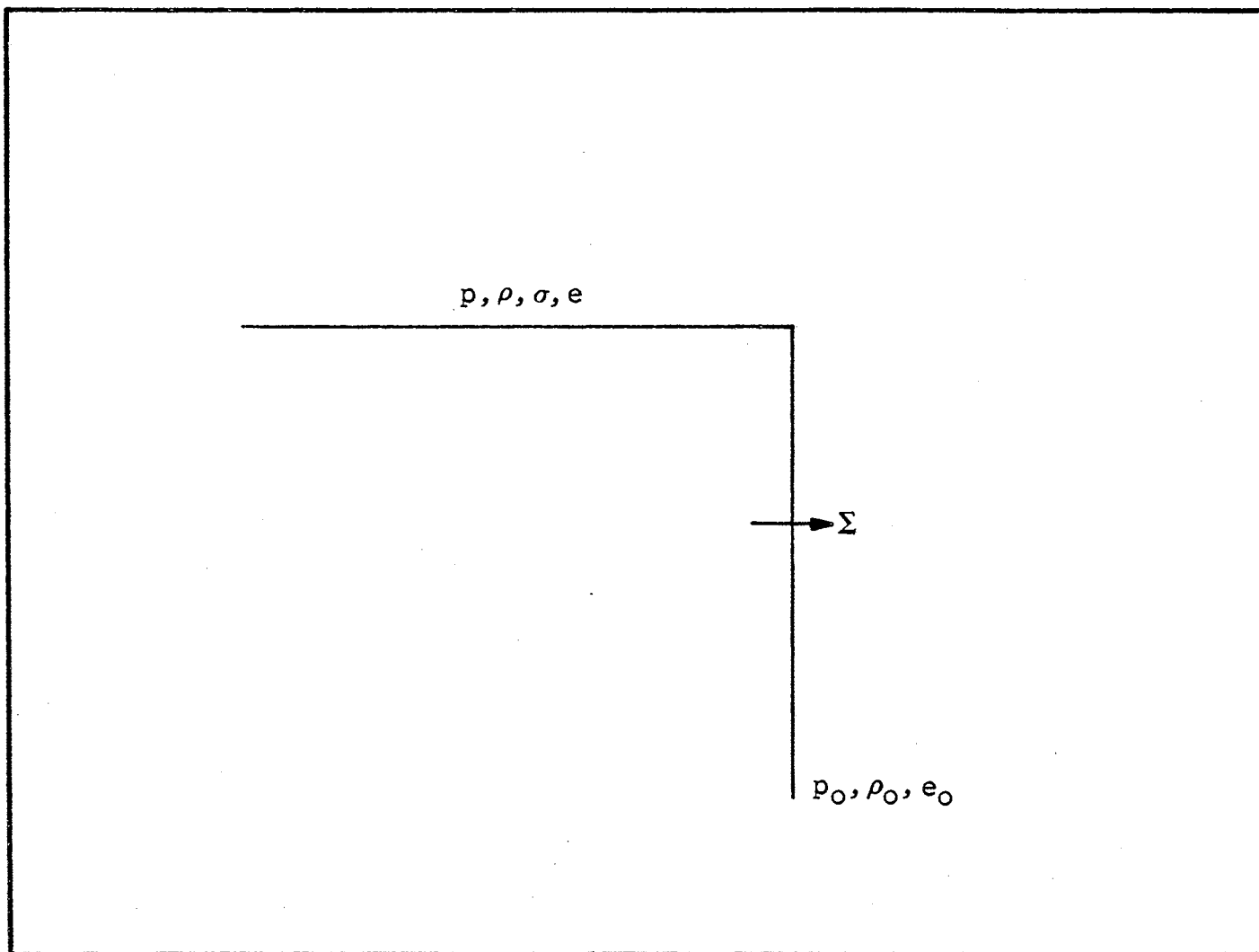


FIGURE 1. PLANE SHOCK FRONT

where C_0 is the velocity of sound in the uncompressed medium ahead of the shock front. The propagation velocity, σ , for disturbances behind the front is greater than the shock velocity

$$\sigma + c > \Sigma$$

where c is the velocity of sound in the medium behind the shock front. The region of decreasing pressure is referred to a rarefaction wave, or a simple expansion wave. The rarefaction gradually changes the entire profile as the shock progresses.

One further specification must be included in the Rankine-Hugoniot conditions for a strong shock wave. Entropy must increase across the shock front. The passage of a shock wave requires an increase in entropy of the supporting medium. This dissipation is not yet provided in the Eulerian flow equations or the Rankine-Hugoniot equations. Fortunately, this further condition on shock propagation as well as the Rankine-Hugoniot relations can be put into a modified set of partial differential equations directly from the Eulerian flow equations presented above.

The Introduction of Dissipation

Shock surfaces appear in the differential equations as points where the velocity, density, internal energy and other variables of the fluid are discontinuous. The Rankine-Hugoniot jump conditions relate the two sides of the shock

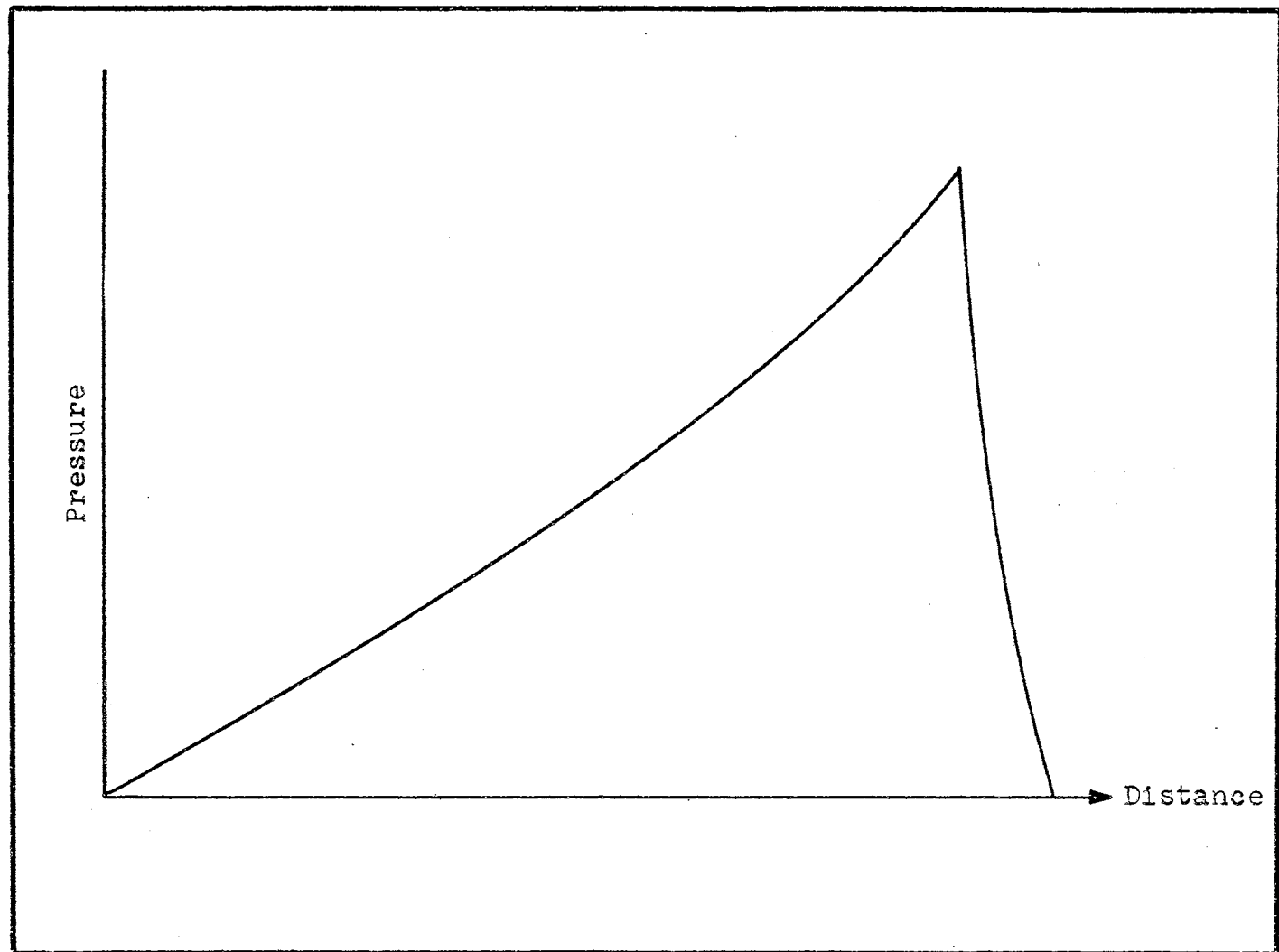


FIGURE 2. TYPICAL PRESSURE PROFILE OF A ONE DIMENSIONAL SHOCK WAVE

front. The Eulerian flow equations provide sufficient conditions for solutions in regions away from both sides of the shock (9). The process of applying the Rankine-Hugoniot conditions as boundary conditions on the flow equations; and thereby, solving the problem of the propagation of a shock wave is known as shock fitting.

J. von Neumann and R. D. Richtmyer (10), in order to avoid the difficulties inherent in solving two sets of conservation equations, devised a method of automatically handling shock motion in the numerical solution of the differential equations. Their method treats shocks automatically in a digital computer. It is based on the introduction of an artificial dissipative mechanism which has some analogy to the viscosity and the heat conduction which do exist in real fluids. The introduction of this artificial, dissipative mechanism, or pseudo-viscosity, into the differential equations tends to smear the shock wave and change it from a discontinuity to a short region in which the variables change rapidly, but continuously. Even though this method does away with explicit application of the boundary conditions, the Rankine-Hugoniot conditions still hold across the shock and the approximation of smearing out the shock can be made to represent a transition zone as accurately as desired by limiting the width of the shock.

The artificial dissipative mechanism is introduced in the form of a pseudo-viscosity term which can be added to the pressure. Originally a term proportional to the square of the velocity gradient was used. Practical tests and analyses carried out by Landshoff (11) indicate that a linear combination of terms proportional to the first and second powers of the velocity gradient gave better results in the numerical calculation of shock problems. A similar expression has been used in the present work. The dissipation is designated as q and is given by

$$q = -C_1^2 \nabla \cdot \vec{V} (C_2 + |\nabla \cdot \vec{V}|) \quad 2.13$$

where C_1 and C_2 are disposable constants. Setting $C_2 = 0$ would give the original von Neumann-Richtmyer equation. In the polar frame of reference, q is

$$q = -C_1^2 \left(\frac{\partial(r^2 u)}{r^2 \partial r} + \frac{\partial(\sin \theta w)}{\sin \theta r \partial \theta} \right) \cdot \left(\left| \frac{\partial(r^2 u)}{r^2 \partial r} + \frac{\partial(\sin \theta w)}{\sin \theta r \partial \theta} \right| + C_2 \right) \quad 2.14$$

The Eulerian flow equations are easily converted to their new form by replacing p by the sum of p and q .

The modified equations describe, not only isentropic flow; but also allow the description of large fluid motions such as shock waves. The theoretical formulation of the hydrodynamic model is complete except for a relation between the pressure and other fluid parameters. A

thermodynamic equation of state which is valid at high pressures will be presented in the next section. This will allow the statement of the problem in a consistent set of equations which can be solved by the numerical method of finite differences.

The High Pressure Equation of State

The construction of an extended equation of state in the relatively low pressure range is based on the evaluation of the Hugoniot pressure, and the Gruneisen ratio from experimental information. The best source of data is from the work at Los Alamos. Walsh, Rice, and McQueen (12) have performed numerous shock wave experiments with many materials.

Theoretical consideration is needed to extend the equation of state into the multi-megabar regions. It is believed that at pressures greater than approximately twenty megabars, the Fermi-Thomas-Divac (13) method yields reasonable pressure, volume, temperature relations.

The gap between low and very high pressures is filled by interpolation. Such a procedure has been used by Tillotson.(16). The form of the equation for density states

$\rho > \rho_0$, where ρ_0 is the normal (STP) value, is

$$p = \left[a + \frac{b}{\frac{1}{\rho^2/\rho_0} + 1} \right] + A(\rho/\rho_0 - 1) + B(\rho/\rho_0 - 1)^2 \quad 2.15$$

where I_0 is the specific internal energy corresponding to ρ_0 . The constants a , b , A , and B are different for each material.

The existence of an adequate equation of state now allows the collection of the equations which describe the proposed impact model. These will be put in a convenient form for numerical solution.

Dimensionless Differential Equations

For convenience in using a computer, all variables are scaled to prevent production of numbers outside the capability of the computer. The choice of a reference scale is the first step in reducing the set of relations to a dimensionless form. This length, α , will be related to the size of the impinging micrometeoroid

$$\alpha = f(r_m) \quad 2.16$$

where r_m is the radius of the projectile. Radial distances are now measured in units of r/α ,

$$R = r/\alpha \quad 2.17$$

Other variables are similarly made dimensionless.

$$\begin{aligned} D &= \rho/\rho_0 & Q &= \theta/\theta_0 \\ P &= p/p_0 & \Phi &= \psi/\psi_0 \\ U &= u/c_0 & W &= w/c_0 \\ E &= I/I_0 \end{aligned} \quad 2.18$$

The values of ρ_0 and p_0 are chosen quite arbitrarily.

The quantities c_0 , I_0 , and Ψ are related to ρ_0 and p_0 .

The independent variable, t , is changed to the new parameter, T , by the relation,

$$T = c_0 t / \alpha \quad 2.19$$

The angular variable, Θ , is dimensionless.

The definitions in equations 2.16 - 2.19 can be substituted into the fluid equations that were given previously. The equation for conservation of mass becomes

$$\frac{\partial D}{\partial T} = - \frac{\partial (R^2 D U)}{R^2 \partial R} - \frac{\partial (\sin \Theta D W)}{\sin \Theta R \partial \Theta} \quad 2.20$$

The equations for conservation of momentum are now written

$$\begin{aligned} \frac{\partial (C D U)}{\partial T} = & - \frac{\partial (P+Q)}{\partial R} - \frac{\partial (R^2 D U U)}{R^2 \partial R} + \frac{D W^2}{R} \\ & - \frac{\partial (\sin \Theta D W U)}{R \sin \Theta \partial \Theta} \end{aligned} \quad 2.21$$

and

$$\begin{aligned} \frac{\partial (C D W)}{\partial T} = & - \frac{\partial (P+Q)}{R \partial \Theta} - \frac{\partial (R^2 D W U)}{R^2 \partial R} - \frac{D W W}{R} \\ & - \frac{\partial (\sin \Theta D W W)}{R \sin \Theta \partial \Theta} \end{aligned} \quad 2.22$$

These were made dimensionless by choosing C_0 so that

$$C_0^2 = p_0 / \rho_0$$

The conservation of energy equation can be expressed in terms of the new variables if I_0 and ψ_0 are subject to the following condition,

$$I_0 = \Psi_0 = P_0 / \rho_0 = C_0^2$$

The new equation is

$$\begin{aligned} \frac{\partial(D\Psi)}{\partial T} = & - \frac{\partial(R^2(P+Q)U)}{R^2 \partial R} - \frac{\partial(R^2 D U \Psi)}{R^2 \partial R} \\ & - \frac{\partial(R(P+Q) \sin \Theta W)}{R \sin \Theta \partial \Theta} - \frac{\partial(\sin \Theta D W \Psi)}{R \sin \Theta \partial \Theta} \end{aligned} \quad 2.23$$

The equation of state is simply transformed.

$$P = \left[.5 + \frac{1.63}{7.813 E/D^2 + 1} \right] \frac{E}{D} + 752(D-1) + 650(D-1)^2 \quad 2.24$$

The constants, $-C_1^2$, and C_2 , are chosen empirically to provide the correct order of magnitude for the viscous pressure term, rather than to fulfill theoretical relations to other parameters.

$$Q = -C_1^2 Y (|Y| + C_2) \quad 2.25$$

where

$$Y = \frac{\partial(R^2 U)}{R^2 \partial R} + \frac{\partial(\sin \Theta W)}{R \sin \Theta \partial \Theta}$$

With the equations in the desired dimensionless form, it is now necessary to convert them to difference equations. In the next chapter, the required difference equations will be obtained.

CHAPTER III

THE NUMERICAL METHOD

A consistent set of equations was obtained in the last chapter, which govern the space and time dependence of the material functions in the microparticle and the target. It is now necessary to solve these simultaneous equations.

There is no known analytic solution for this system of equations, and it is not anticipated that one will be found in the immediate future. (15). The highly developed state of electronic computers, such as the IBM - 7090 or IBM - 7094, makes the use of numerical methods feasible for reasons of both time and relative simplicity of processing. A well-posed, initial-value problem in fluid mechanics may be formulated and the method of finite differences employed to convert the differential equations to algebraic difference equations. These difference equations may be readily solved on the large computers.

The Two Dimensional Difference Equations

The problem for solution has spherical symmetry and, for this reason, the equations for solution were converted to spherical coordinates. Since the problem has symmetry, a vertical impact may be followed, after a judicial selection

of coordinates, by plots on only a part of one quadrant in a single plane. The coordinates are R and Θ . For a normal impact, the axis of R for $\Theta = 0$ is taken vertically through the initial point of contact between the microparticle and the surface of the semi-infinite slab. The origin of coordinates, at which $R = 0$, is taken at a little more than twice the diameter of the microparticle above the point of initial impact. The plot of the entire affected volume of the impact is obtained by rotating the selected plane mentioned above the vertical line R for $\Theta = 0$. The region of impact on the plane is divided into a number of cells. The equations are differenced for this mesh. Individual cells are designated in space by M in R direction and L in the Θ direction; so that,

$$M = 1, 2, 3, \dots, M_{\text{final}} = MF$$

$$L = 1, 2, 3, \dots, L_{\text{final}} = LF$$

The time is measured in units of $N \cdot DT$, where DT is a small but finite increment. The radius at the center of each cell is given by

$$R_M = R_0 + DR \cdot (M - .5)$$

and at the sides of a cell by

$$R_{M-\frac{1}{2}} = DR \cdot (M - 1), \quad R_{M+\frac{1}{2}} = DR \cdot M + R_0$$

The other two boundaries of a cell are rays of constant angle, which are separated by a constant, $D\Theta$. The area of any cell at a distance, R_M , from the origin is

$$AA_M^L = R_M \cdot DR \cdot D\theta$$

Values of the density, the pressure, the pseudo-viscosity, the two components of the material velocity, and the energy are defined at the center of each cell and are regarded as average properties of the material within a cell. Each variable is designated as f_M^L . This identification follows from above and refers to cell number M along R and the cell number L in the θ direction. These values of the quantities stored for each mesh point advance by a small, later time, DT .

Forward time differences are used for all time derivatives and all spatial derivatives are initially written in terms of central differences. Equation 2.20 can now be written as

$$\frac{D_M^{L,N+1} - D_M^{L,N}}{DT} = - \frac{R_{M+1/2}^{2L,N} D_{M+1/2}^{L,N} W_{M+1/2}^{L,N} - R_{M-1/2}^{2L,N} D_{M-1/2}^{L,N} W_{M-1/2}^{L,N}}{R_M^2 DR} - \frac{\sin \theta_M^{L+1/2,N} D_M^{L+1/2,N} W_M^{L+1/2,N} - \sin \theta_M^{L-1/2,N} D_M^{L-1/2,N} W_M^{L-1/2,N}}{R_M D\theta \sin \theta_M^L}$$

To compress notation, see Figure 3, quantities at $M, L - \frac{1}{2}$ are designated side one, at $M - \frac{1}{2}, L$, side two; at $M, L + \frac{1}{2}$, side three; and at $M + \frac{1}{2}, L$, side four. Using this shorthand and factoring AA_M^L in the denominator, the finite difference form for the conservation of mass equation becomes

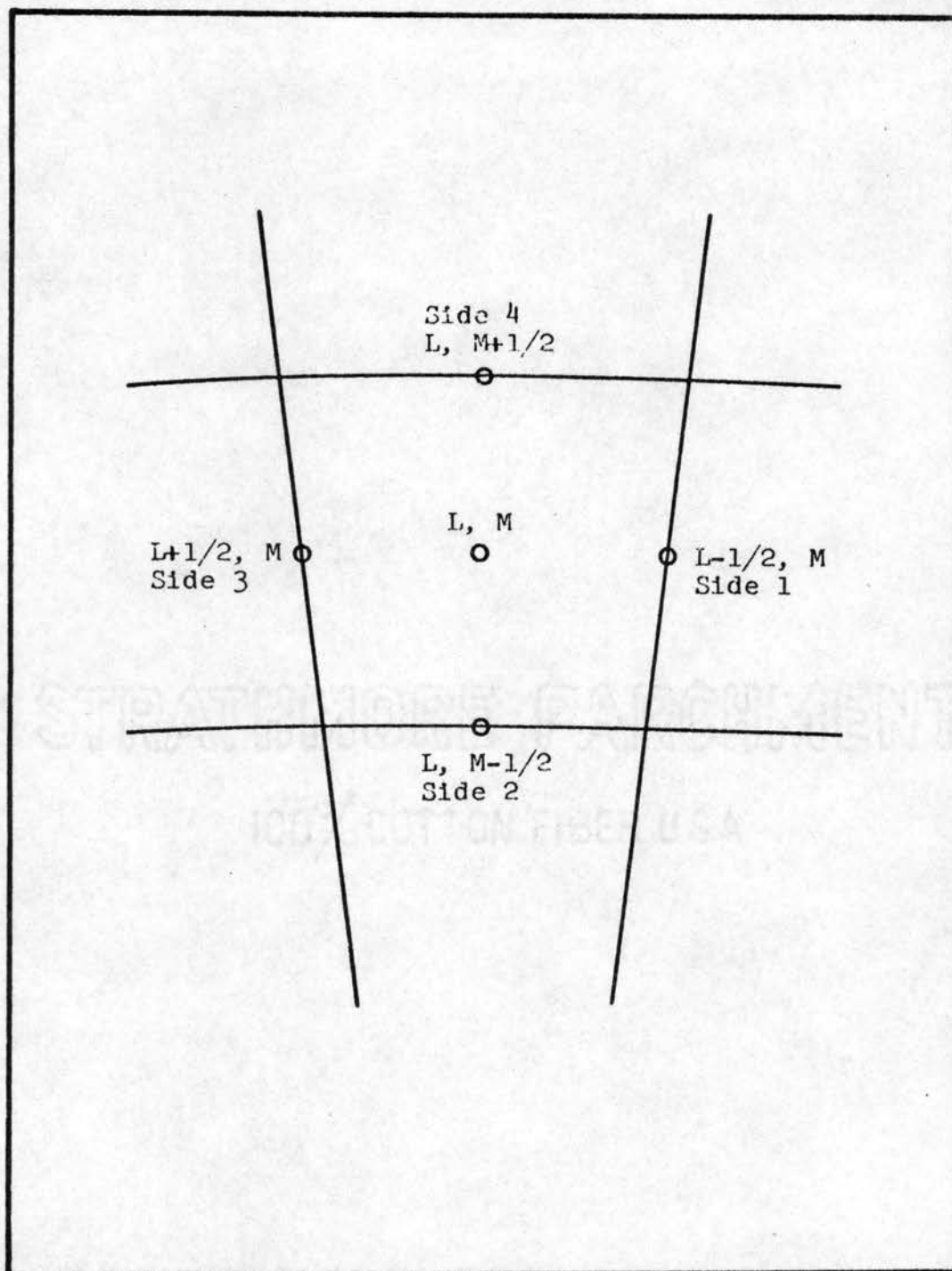


FIGURE 3. CELL BOUNDARY NOTATION

$$D_M^{L, N+1} = D_M^L + \frac{DT}{AA_M^L} [D\theta/R((R^2 DW)_2 - (R^2 DW)_4) + DR/\sin\theta((\sin\theta DW)_1 - (\sin\theta DW)_3)] \quad 3.1$$

All quantities on the right are for time $N \cdot DT$. If these are all known, or prescribed, then the density, $D_M^{L, N+1}$, for the time $(N+1) \cdot DT$ can be calculated.

The other conservation equations are treated similarly.

Radial equation of motion:

$$(DW)_M^{L, N+1} = (DW)_M^L + \frac{DT}{AA_M^L} [R \cdot D\theta((P+Q)_2 - (P+Q)_4) + D\theta/R((R^2 DW)_2 W_2 - (R^2 DW)_4 W_4) + DR/\sin\theta((\sin\theta DW)_1 W_1 - (\sin\theta DW)_3 W_3) + DR \cdot D\theta D_M^{L, N+1/2} W_M^{L, N+1/2} W_M^{L, N+1/2}] \quad 3.2$$

Tangential equation of motion:

$$(DW)_M^{L, N+1} = (DW)_M^L + DT/AA_M^L [DR((P+Q)_1 - (P+Q)_3) + DR/\sin\theta((\sin\theta DW)_1 W_1 - (\sin\theta DW)_3 W_3) - DR \cdot D\theta \cdot D_M^{L, N+1/2} L_M^{L, N+1/2} W_M^{L, N+1/2} + D\theta/R((R^2 DW)_2 W_2 - (R^2 DW)_4 W_4)] \quad 3.3$$

Conservation of energy:

$$(D\Psi)_M^{L, N+1} = (D\Psi)_M^L + DT/AA_M^L [DR/\sin\theta(-(P+Q)_1 W_1 \sin\theta_1 - (P+Q)_3 W_3 \sin\theta_3 + (\sin\theta DW)_1 \Psi_1) + D\theta/R((R^2 DW)_2 \Psi_2 - (R^2 DW)_4 \Psi_4) + R(P+Q)_2 W_2 - R(P+Q)_4 W_4] \quad 3.4$$

The two auxiliary equations are independent of time and are algebraically translated.

The above system of equations is explicit and the solution may be moved forward, continuously, by means of simple algebra. Equation 3.1 gives a value for the new density, which is then used to find the new velocities from equations 3.2 and 3.3. Continuing with these known values, internal energy is found from equation 3.4. At the new time level, the quantities D^{N+1} , E^{N+1} , U^{N+1} , and W^{N+1} enable the additional equations to be solved for new values of the pressure, P , and the pseudo-viscosity, Q . The new profiles (set of values $f_M^{L, N+1}$) then become the starting point for the next advance in time.

An extensive discussion of means of evaluating difference expressions is available in a previous work. (14). The selection of means for evaluating all terms in the modified flow equation provides an algebraic procedure very straightforwardly programmed for a digital computer. Then the equations will yield a solution for two-dimensional, fluid motion, including shock waves and other large-scale fluid movements.

Finite Difference Mesh Configuration and Cycling

The selection of a single plane to illustrate the solution and to provide the net that is required for the computer solution was discussed earlier in this chapter.

Both the microparticle, before impact, and the free surface of the semi-infinite slab must be included in the plane.

The microparticle is represented by a semicircle of radius R_M . The position of the face of the semi-infinite target is initially given by

$$R \cos \theta = S \quad 3.5$$

where S is a constant distance measured in the same units as R . In such a mesh, there are three possible kinds of cells; cells full of aluminum, empty cells, and mixed cells, which are partially filled with aluminum and partially empty. These mixed cells contain a material - vacuum boundary. Each mixed cell is marked with a parameter called the partial area, A_M^I . It is a quantity which signifies the amount of area of a cell that is filled by aluminum.

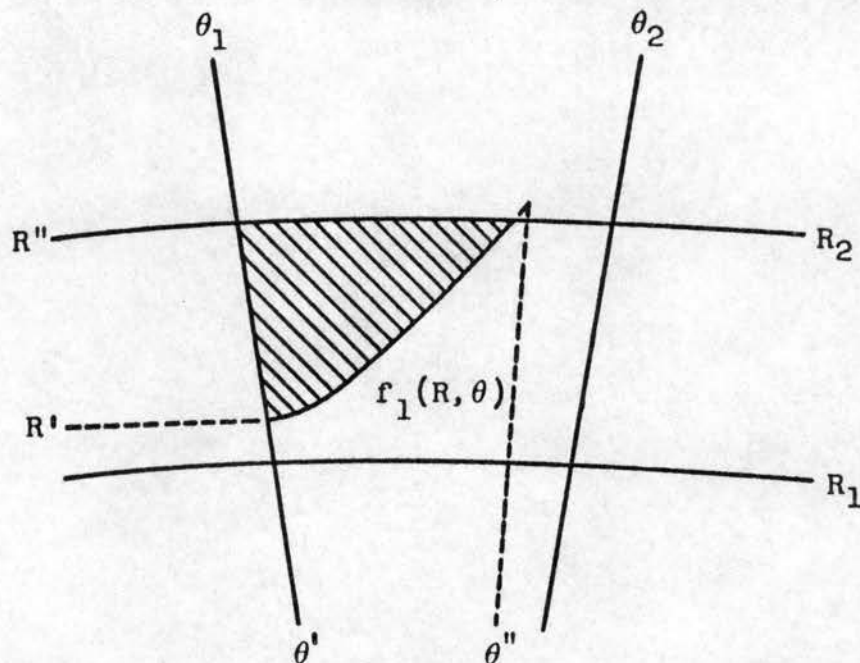
The initial information to the computer program is the free velocity of the microparticle, V_0 , together with the locations and partial areas of the mixed cells.

The circumference of the micrometeoroid is given by the equation of a circle in polar coordinates,

$$b^2 - a^2 + R^2 - 2bR \cos \theta = 0$$

where a is the radius of the circle with center at $(b, 0)$.

The partial area of a cell is determined by computing the points of intersection of this equation with the coordinate lines of constant R and constant θ and then by integrating between these limits. This process is illustrated in Figure 4. The diagram shows a typical mixed cell in the



$f_1(R, \theta)$ is the equation of a semicircle.

$R_1, R_2, \theta_1, \theta_2$ are cell boundaries.

$R', R'', \theta', \theta''$ are limits of integration.

$$A = \int_{\theta''}^{\theta'} \int_{R'}^{R''} [R_2 - f_1(R, \theta)] dR d\theta$$

FIGURE 4. INITIAL PARTIAL AREA CALCULATION

lower half of the projectile. There is a sign change for the upper half of the microparticle. These calculations were made independently of the main computer program on an IBM-650.

The motion of the microparticle as well as the boundary of the target is followed by changing the partial areas in the mixed cells and by the appearance and disappearance of mixed cells. The fluid parameters of a mixed cell are calculated in the manner that is outlined, above, for aluminum cells is that of changing the partial areas in time. Perhaps the simplest possible method is to use an approximate formula based on the known velocity components.

$$A_M^{L\ n+1} = A_M^L - \Delta R \cdot \Delta \theta \quad 3.7$$

where

$$\Delta R = U_M^L \cdot DT$$

$$\Delta \theta = W_M^L \cdot DT$$

where DT is the elapsed time of one iteration cycle.

The calculation of the new partial areas is the last step of a calculation cycle. The whole mesh has been moved forward by a time step, DT. The mixed cells, which may contain a moving boundary, must be changed from time to time. A test must be made after the end of each time step to ascertain whether any of the mixed cells should be replaced by either a full, or an empty cell. Either possibility

requires the construction of a new mixed cell. The partial area of a mixed cell might be calculated greater than the actual area of the cell, or as vanishingly small. In both cases, the cell is changed.

In summary, the solution is obtained as follows, the values of all parameters are found by successive applications of equations 3.1 through 3.4 for all full and mixed cells. The parameters of an empty cell cannot be changed by these equations. Empty cells are changed only by movements of mixed cells. Then, the new partial areas are found and mixed cell changes are made, if necessary. This procedure can then be repeated to give a numerical solution for the whole region as time increases with each calculation cycle.

Quality of Solutions

There are two important questions to be asked concerning the accuracy of a numerical solution to an initial value problem. (18):

1. Do both the partial differential equations and the difference equations possess unique solutions?
2. If the answer to 1 is yes, is the solution that is obtained by solving the difference equations, step by step, actually a sufficient approximation to the true solution?

Full and completely rigorous answers to these questions are not available. A unique solution is judged to exist if the physical problem is well defined. It is generally believed that the compressible fluid equations give rise to a system of partial differential equations which define as well-posed, initial-value problem. (19).

The second question concerns the convergence of the approximate solution to the true solution. The true solution is not known for comparison. The system of difference equations is examined, somewhat empirically, for convergence. Different combinations of the increments, ΔR , $\Delta \theta$, and ΔT are used and the resulting solutions are compared. If these different solutions agree very closely, then a good solution is probably being obtained.

A more encouraging condition can be suggested from the Equivalence Theorem of Lax (20):

Given a properly posed initial value problem and a finite-difference approximation to it that satisfies the consistency condition, stability is the necessary and sufficient condition for convergence.

The consistency condition requires that the resulting numerical solution depend continuously on the initial data and that the difference equations go over to the differential equations as ΔT , ΔR , and $\Delta \theta$ approach zero. The first part of the condition is satisfied by the mechanism of the finite difference method by which the solution progresses from the known to the unknown. The second part of the consistency condition is satisfied, since this is the usual method of

deriving the hydrodynamic flow equations. With the idea established that stability implies convergence, the concept of stability will be examined.

Since numerical approximation methods are used, it is expected that there is a small difference between the true solution and the computer solution,

$$\epsilon = f(R, \theta, T) - f(M \cdot \Delta R, L \cdot \Delta \theta, N \cdot \Delta T)$$

The solution is stable if this error remains small or grows smaller. The solution is unstable if ϵ grows without limit. When the computer results indicate profiles with exceptional, oscillatory behavior, the particular solution can be corrected by the proper choice of the mesh ratio,

$$\Delta \vec{X} / \Delta T. \quad (21). \quad \text{The position vector is } \vec{X} = [R, \theta].$$

One well-known relation in the field of fluid dynamics is the Courant condition (22),

$$\Delta \vec{X} / \Delta T = c_m > c$$

that is, the mesh speed c_m must be greater than the sound speed which is the greatest velocity at which disturbances may be propagated from place to place in an elastic medium. For problems involving shocks and large material velocities, this restraint is insufficient.

Richtmyer (22) has shown for some cases a more suitable requirement is

$$c_m > c + |\vec{V}|$$

where \vec{V} is the material velocity. This condition recognizes that disturbances move with the velocity of sound plus the

velocity of the flowing medium.

In the problem to be discussed, the medium is usually highly compressed. The flow velocity and the sound velocity are roughly of the same order of magnitude. The following approximation, then is made to the above condition,

$$\Delta \vec{X}/DT \approx 2\vec{V}$$

In one-dimensional tests, however, this relation prescribed a mesh ratio which was about five times too large. (14).

In practice, DR and $D\theta$ are fixed and DT is varied to satisfy requirements for stability. The actual condition used to check stability is written

$$DT \leq .1 \sqrt{(DR)^2 + R_0^2 (D\theta)^2 / (U^2 + W^2)} \quad 3.8$$

where U and W are the maximum flow velocity components occurring in the solution and R_0 is a typical radius of the finite difference mesh.

Development of Computer Program

The computer code for solving the finite difference equations was written for an IBM-7090 computer. The size of the computer was demanded by the requirement that an accurate numerical approximation of the solution be obtained. In the radial direction, the net was marked by fifty cells. In the angular direction, there were initially thirty-five cells covering a sector of 35° . The IBM-7090 has a storage capacity of approximately 32,000 words. Of this storage,

about 25,000 words were used for storage of variables for each point of the finite difference mesh. There were eleven parameters defined and stored for each fluid cell:

D, Density in the cell.

U, radial velocity.

W, tangential velocity.

E, internal energy.

P, pressure.

CU, radial velocity at time N+1.

CW, tangential velocity at time N+1.

CE, internal energy at time N+1.

A, partial area (if any). NT, a name tag denoting the kind of cell; (+) for a full, aluminum cell, (-) for a mixed cell, and (0) for an empty cell.

CD, density in a cell at time N+1.

The computer code was written in FORTRAN and in FAP. FORTRAN is a high level computer language which, with slight changes, is acceptable to a wide assortment of large digital computers. It is not, however, the basic machine language of any machine and must, therefore, be translated into the basic machine language of the computer being used. This is accomplished generally in two steps; the first being a translation to a symbolic assembly language, the second being to assemble the symbolic language program into a basic machine language program. FAP, FORTRAN ASSEMBLY PROGRAM, is the symbolic language associated with Fortran II. The transla-

tion process required by programs written in FORTRAN is less efficient, that is, produces more instructions, than programs written in FAP or a basic binary machine language. In order to conserve storage, part of the computer code 'DRAW', developed to solve the modified flow equations, was written in the symbolic language. The final program occupied about 6,500 words of the computer's memory.

To solve the difference equations on a 7090, a logical calculation path must be developed for use by the computer. This process is illustrated, in a rather general way, by Figure 5. Calculations are performed for each dependent variable in each cell corresponding to the directions of the difference equations. Other monitoring is required and performed by the computer code to check the mesh configuration and impose boundary conditions.

The cycling of the program would be as follows: one first calculates the values at time $N+1$ for the whole mesh using equations 3.1-3.4 for all full and mixed cells. Equation 3.7 is used to find the new partial area for all mixed cells. Boundary cell changes are then made if there are any. The new value of pressure is then found from the equation of state. After the completion of a cycle, the results may, or may not, be printed out under computer program control. The new values for the variables replace the initial values so that the cycle may begin again.

Read in initial values of variables
and constants of program.

Compute Density, Radial and Tangential
Velocity Components, and Specific
Internal Energy for each cell for
one time increment later than starting
conditions.

Compute Q-term and Pressure for every
cell.

Compute change in Partial Areas for
each interface cell. Test interface
cells for cell changes

Write all computed values, if desired.

Store computer values in initial value
locations.

Figure 5. Computer Flow Diagram

CHAPTER IV

DEVELOPMENT AND PRESENTATION OF SOLUTIONS

The set of difference equations developed for a computer solution have sufficient versatility to yield a solution for arbitrary initial values and boundary conditions. The basic initial value necessary for a solution is the free space velocity of the incident micrometeoroid. The physical properties of aluminum under normal conditions supply the further necessary initial value information. Boundary conditions must be applied to the modified flow equations to insure the proper representation of material-vacuum-interfaces and symmetry properties assumed in the problem.

After obtaining the solutions, the numerical data is reduced by selective plotting of the space variation of the fluid variables at different instants of time. This chapter presents a survey of the information obtained by using the hydrodynamic model.

A series of curves illustrating the typical behavior of the pressure, velocity, density, and internal energy are shown as functions of space and time. Further analysis of crater growth and peak pressure decay are also portrayed

graphically. The dominant features of the solutions are the appearance of two shock waves at the point of initial contact and the formation of a cavity behind the penetrating projectile. Flow patterns peculiar to the spherical shape of the incident micrometeoroid are also displayed.

Initial Values

The basic operation of the finite difference method consists of moving from the known to the unknown. A completely specified net at one time is advanced by a small step in time. The action is then repeated indefinitely to develop a numerical solution. To start the solution, at time equal zero, a simple configuration is chosen. Just prior to the beginning of the calculations, the leading point of the micrometeoroid is in contact with the semi-infinite target. This is called the point of impact and lies on an axis normal to the target. The material velocity of the projectile is identical with its free space velocity, V_0 . The material of the target is at rest. Both projectile and target are considered to be inviscid fluids during the flow that follows the impact. The density of both bodies is that of normal aluminum. Other fluid parameters such as the internal energy and pressure are initially zero.

Figure 6 illustrates the prescribed conditions.

In addition to these initial values, further conditions must be applied during the running of the computer program.

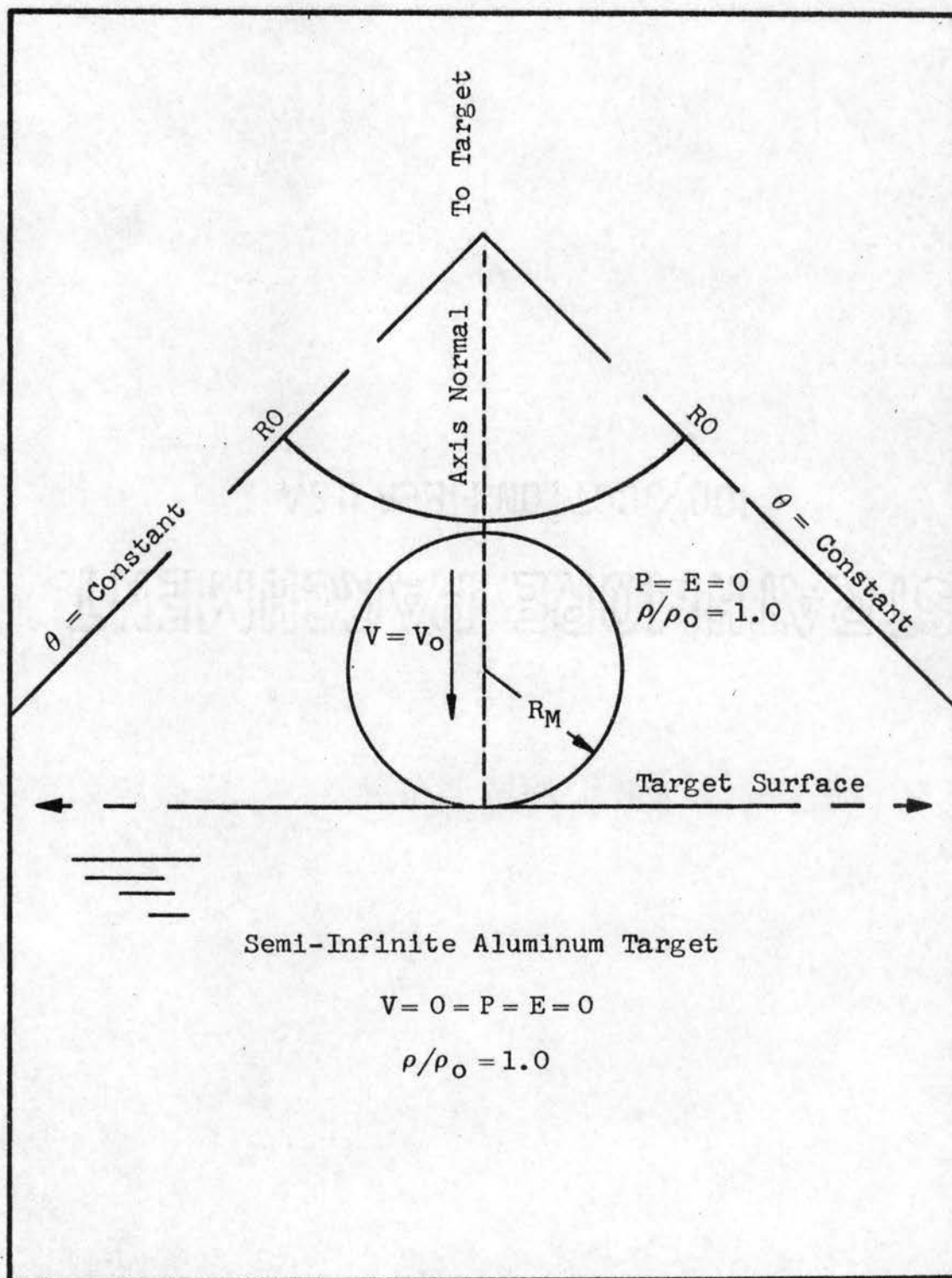


FIGURE 6. INITIAL VALUE ILLUSTRATION

Boundary Conditions

Several boundaries appear in the formulation of the impact problem. Each must be subject to specialized treatment. The region of interest is taken as a sector of one quadrant (see Figure 6) of a polar coordinate system with the variables R and Θ . The initial point of contact is on the axis. The application of this condition is accomplished by requiring that no mass flow across this axis. A material-vacuum interfact requires specification of zero pressure on such a line. This is accomplished with respect to the finite difference mesh by setting the pressure in a cell containing some aluminum material and some empty space equal to zero on the side or sides of the cell adjacent to the vacuum. Apart from this restriction of no applied force, the aluminum-vacuum boundaries are free to move and are moved as indicated by the velocity of the solid material in the mixed cell. As materials flows out, density cannot be less than in the original solid. The computer program also monitors the differencing schemes to prohibit averaging across an interface. Fluid properties are not averaged between empty and full cells.

The Solutions

The finite difference method that is described in the previous chapter, complemented by the necessary initial conditions and boundary specifications was used to obtain solutions for the hydrodynamic model. The numerical results evaluate the density, the pressure, the specific internal energy, and the two components of the material velocity at cell centers; that is, these variables as functions of R and θ , at discrete instants of time. The quantity of numerical data produced by the computer is enormous. The description provided by the hydrodynamic model is best shown in the form of graphs which show the preceding variables at selected instants as the impact proceeds in time. The following sections give illustrations of the important results and the nature of the solutions.

Organization of Solutions

The step by step description of the early progress of the hypervelocity impact are first illustrated graphically by profiles which show the variation of pressure along the normal axis to the target at different times. Two dimensional plots are shown in a plane bounded by the axis of symmetry. The volume distribution of the variables is obtained by rotating the two dimensional plots around the normal axis. The values at an instant of time are shown by

lines of constant density, by isobars, by lines of constant energy, and by arrows that show the magnitude and direction of the velocity. Since the volume distributions of all the variables is symmetric about the axis of symmetry, the velocity is entirely contained in the two dimensional plot.

The illustrations presented show the initiation of shock waves at the point of impact and subsequent decay as larger volumes and free surfaces are encountered. Flow patterns for the pressure and material velocity are presented with comments on the chief features. Graphs of the time history of free surface motion are then presented.

Shock Wave Formation and Decay

The most noticeable features of the hydrodynamic solutions are the two shock waves which originate from the point of initial contact. Two compressive waves of approximately equal strength appear soon after the start of the calculations. One moves into the target and the other into the projectile. The shock wave into the micrometeoroid is reflected from the vacuum-material boundary as an expansion wave which races to weaken the primary shock wave traveling into the target. This primary wave also decays as the volume it affects increases. As the primary front penetrates greater distances into the target, more and more material is compressed which decreases the energy density in the propagating disturbance.

Pressure Profiles

The processes of shock wave formation and subsequent decay are illustrated in the first series of graphs, in Figures 7, 8, and 9. To amplify the points of discussion, shock profiles, which are curves of function values versus distance, are presented for several different times along a line near an axis normal to the target. The motion of the fluid is very nearly one dimensional along such a line. On the axis, variables are functions of the radial distance. Each Figure is marked along the distance scale in units of the micrometeoroid radius, R_M . The distance is marked from the point of initial contact, S. In those graphs in which the back edge of the micrometeoroid or back edge of the fluid material is contained, the position is labeled with the letter B. The pressure is given in units of megabars. Each megabar is approximately one million atmospheres. Plots of the pressure illustrate graphically the growth of the affected volume which occurs after impact. An initial peak, slightly displaced below the point of first contact, indicates the start of shock wave formation. Approximate wave profiles show the establishment of two shock waves. Reflection and propagation of expansion waves from the vacuum-aluminum boundary, where the pressure is equal to zero, are again seen to contribute to the decay of the primary shock wave.

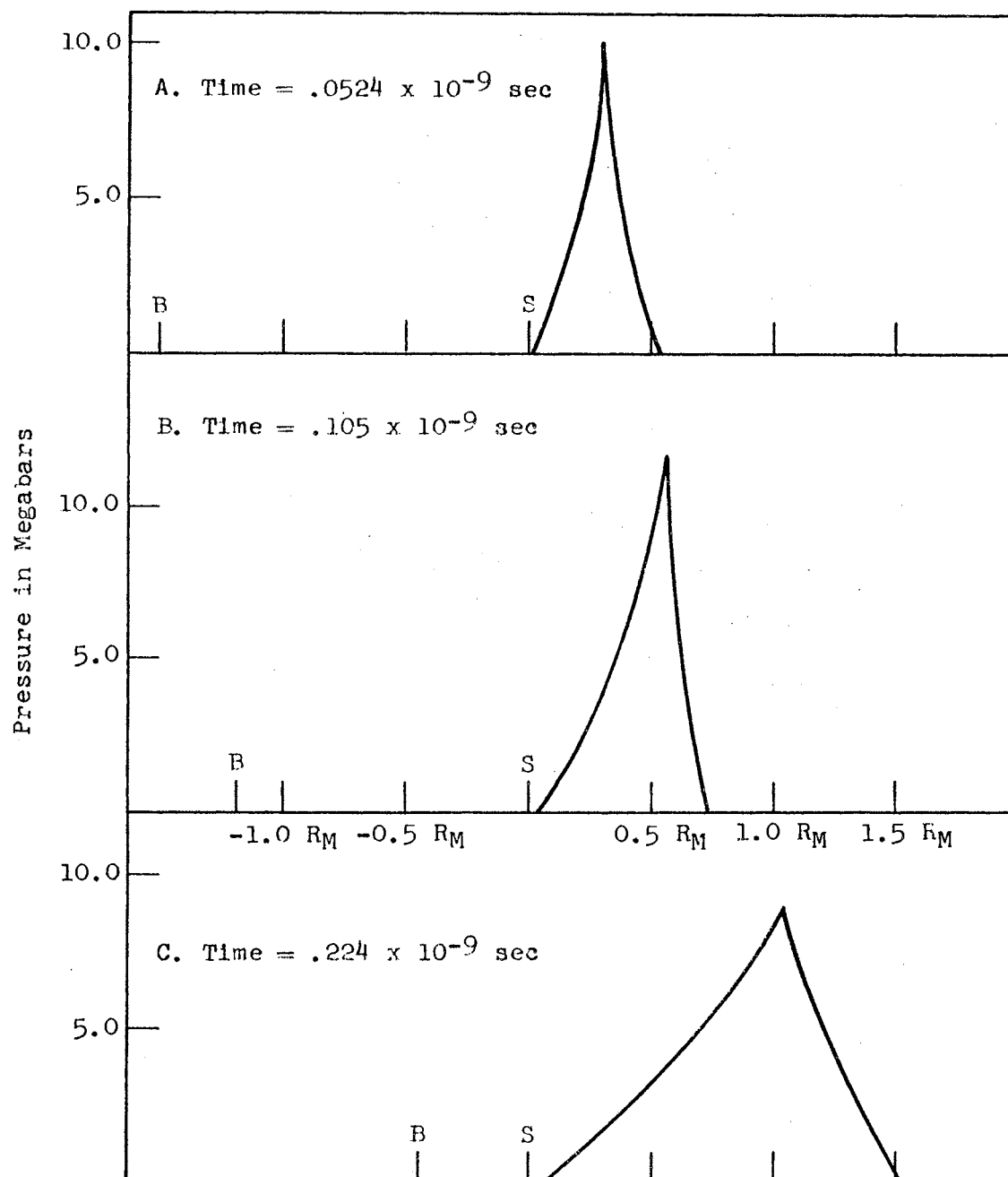


FIGURE 7. PRESSURE PROFILES ALONG NORMAL AXIS

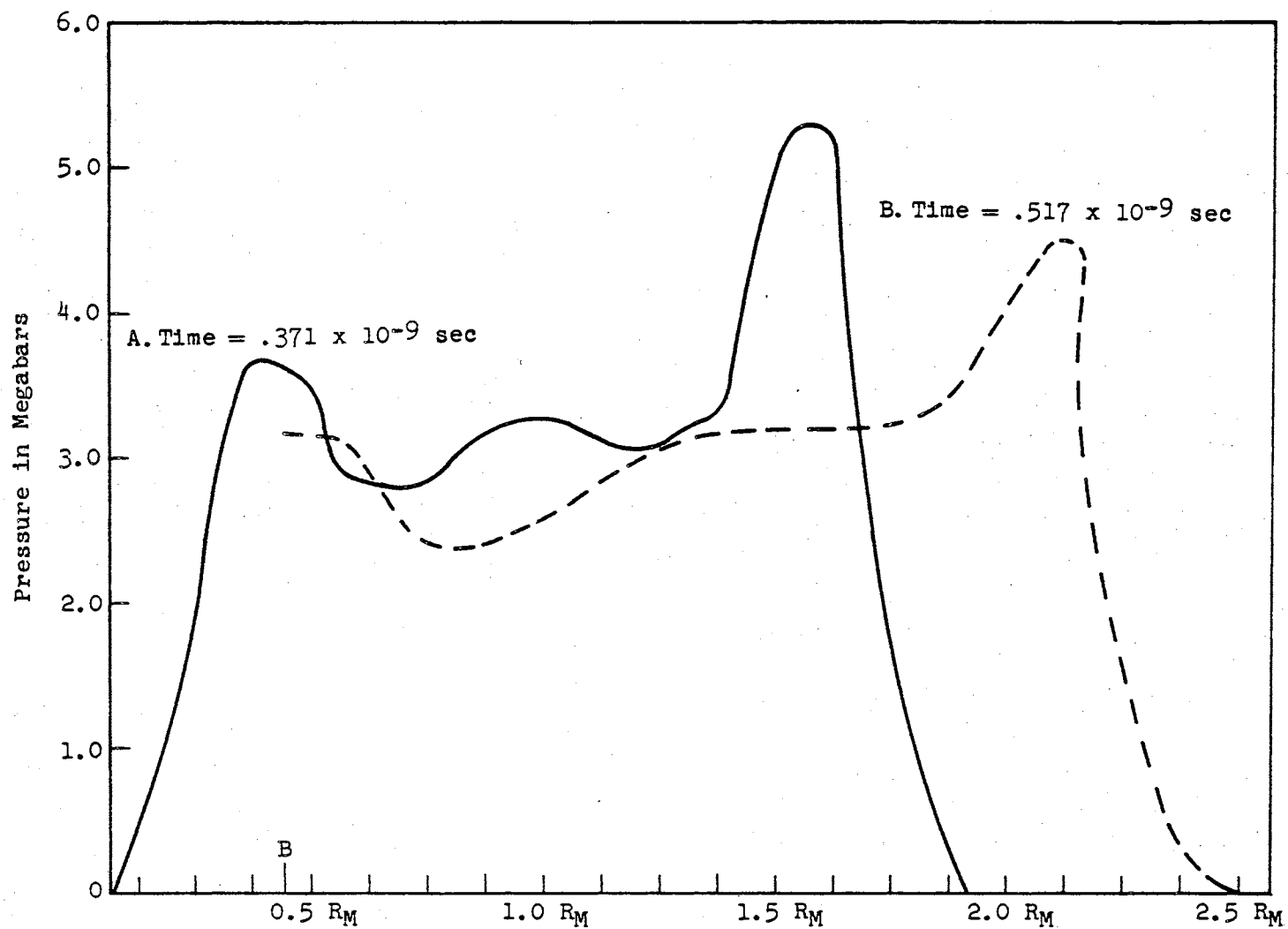


FIGURE 8. PRESSURE PROFILES ALONG NORMAL AXIS

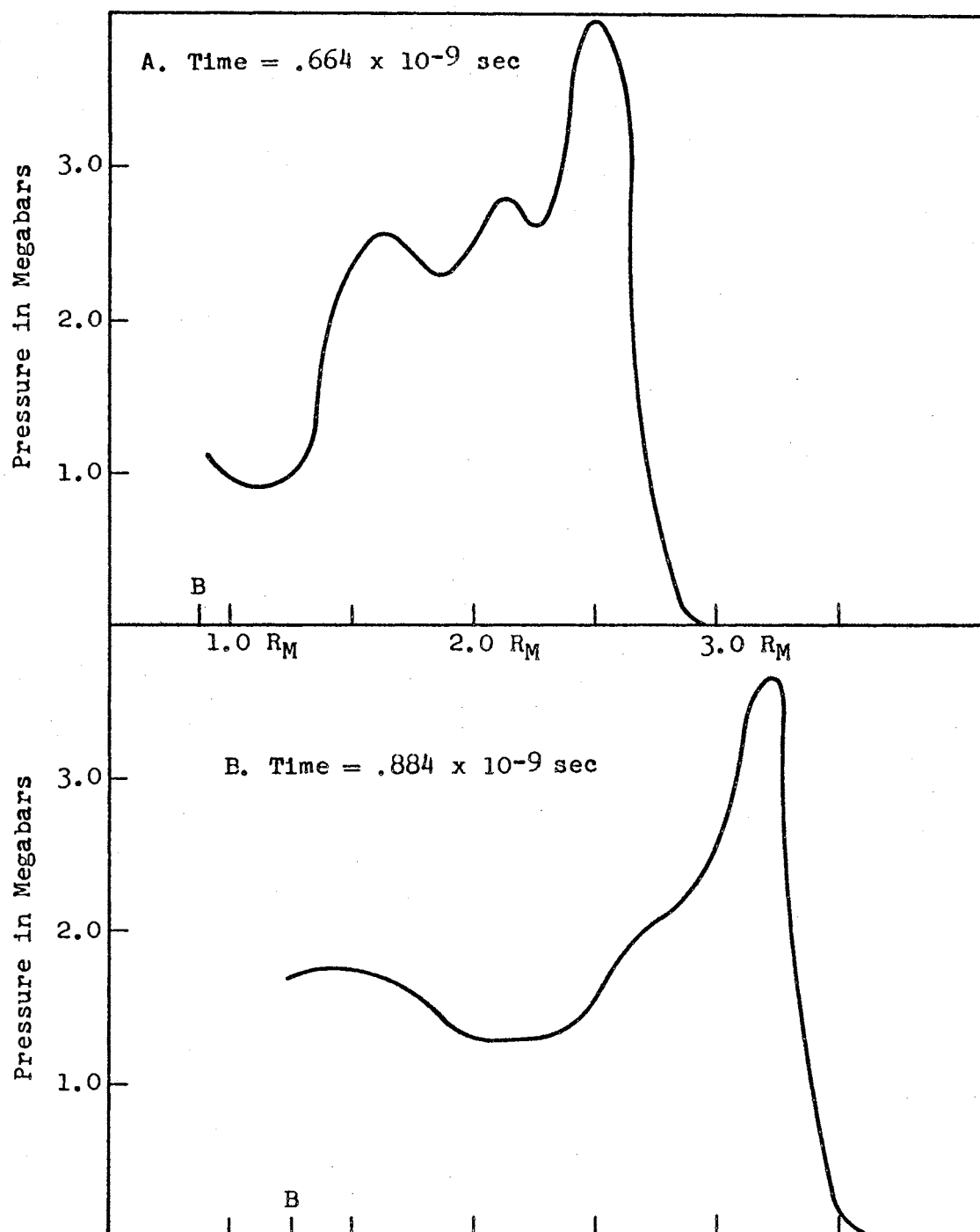


FIGURE 9. PRESSURE PROFILES ALONG NORMAL AXIS

Early stages of pressure development are illustrated in Figure 7. The first results given by the finite difference scheme are for only a few cells of the mesh and must be interpreted as containing oscillations.

Reflection of a strong pressure front from the free surface will begin soon after the time profile shown in Figure 8-A. This release wave combined with declining peak pressures at the head of the disturbance can be seen in Figures 8-B and 9. In the pressure curves, there seems to be a spurious peak at the front of the shock wave; that is higher pressures than would be expected. This is due in part to the effect of the pseudo viscosity in the numerical calculation. The value of the coefficients in the expression for the pseudo viscosity were kept at very small values, with greater smoothing effects on the flow profiles being obtained from the structure of the finite difference equations. This was done to avoid losses in moving the particle through the cells of the finite difference mesh. The reduction in value of the pseudo viscosity results in larger oscillations in the variables, particularly the pressure and the specific internal energy, than in previous hydrodynamic calculations. (4,14).

Full two dimension results of the hydrodynamic model are shown in the next section.

Two Dimensional Distributions

The hypervelocity impact of a micrometeoroid on a semi-infinite target puts the material of the target in motion and produces a large scale disturbance of the flowing aluminum. A series of two dimensional maps showing the fluid pressure and material velocity distribution drawn from the numerical solutions of the hydrodynamic model are presented in this section.

A qualitative survey of the features associated with hypervelocity impact has been given by Charters (8). This description will be discussed now since the present solution embodies a number of observed effects.

The impact is accompanied by a flash of light. Radiation can be observed from the immediate vicinity of the impact. This is not shown by the hydrodynamic equations since they contain no radiation producing mechanism. If the governing equations were supplemented by an equation of state which includes ionization and radiation energy, and changes in the conservation equations, it is believed that the plasma state formed by the impact would give radiation.

The shock waves discussed are observed in high speed experiments. One, referred to as the primary shock wave, radiates out from the point of impact, compressing and accelerating the material of the target ahead of the on-rushing sphere. Another wave moves back into the projectile.

opposite to the motion of the projectile. The result of these two movements is an approximately stationary shock front moving very slowly beyond the point of initial contact.

As the back edge of the micrometeoroid passes the position of the original target, a depression or crater starts to form. Most of the flow is in a radial direction, but some material moves around the crater edge and is ejected. These features seen in the laboratory are also evident in the numerical solution. The opening of a cavity and the movement of target material above the original target surface are both very striking in the solutions presented.

The shock wave which is reflected from the free surface as a rarefaction wave eventually overtakes the primary shock wave. This latter wave penetrates great distances into the target. The expanding crater follows at a distance. Between the two, a shell of highly energetic matter, compressed by the shock and stretched by the rarefaction, is found. The strength of the shock wave decreases as its volume of action increases, and as it is overtaken by rarefaction waves originating at the free surface of the material. These features of hypervelocity impact are displayed in the hydrodynamic solutions.

Ultimately, the plastic and elastic properties of the target material void the perfect fluid assumptions and the final size and shape of the crater cannot be fixed. This

difficulty can be remedied by consideration of the change from fluid to elastic flow.

Distributions of the pressure and material velocity are shown for different instants of time. The velocity is portrayed by scaled vectors representing the velocity of material at the tail of the vector. A velocity scale is given on each illustration. Pressure contour maps are obtained by connecting points of equal pressure on different radial lines. Distances are shown on the normal axis in units of the micrometeoroid radius, R_M . The times shown for the typical 10^{-9} gm. micrometeoroid.

Pressure and Material Velocity Distributions

The micrometeoroid enters the target quite rapidly. Two early velocity distributions are shown in Figure 10. Most of the velocity vectors are parallel to the axis and represent the free velocity of the micrometeoroid. The vectors near the original surface and below are reduced in magnitude and oscillate.

The pressure distribution in Figure 10-B shows the highest pressure attained in this particular impact case. Two approximately equal shocks will be formed from the pressure peak shown. There is some asymmetry apparent in Figure 10-B and subsequent plots due to the geometry of the entering projectile and the initial division of material velocity. The material of the micrometeoroid has initially

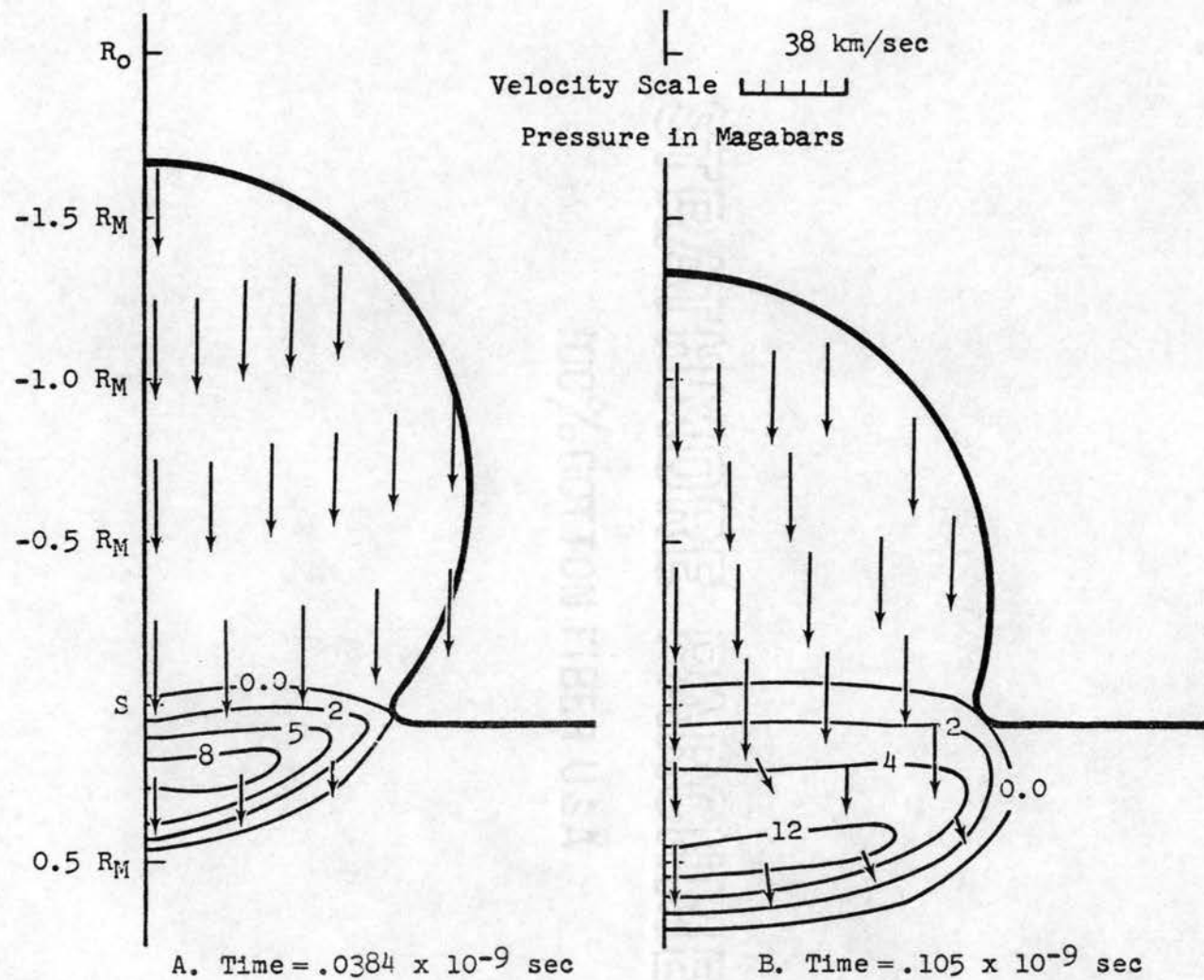


FIGURE 10. PRESSURE CONTOURS AND VELOCITY DISTRIBUTIONS

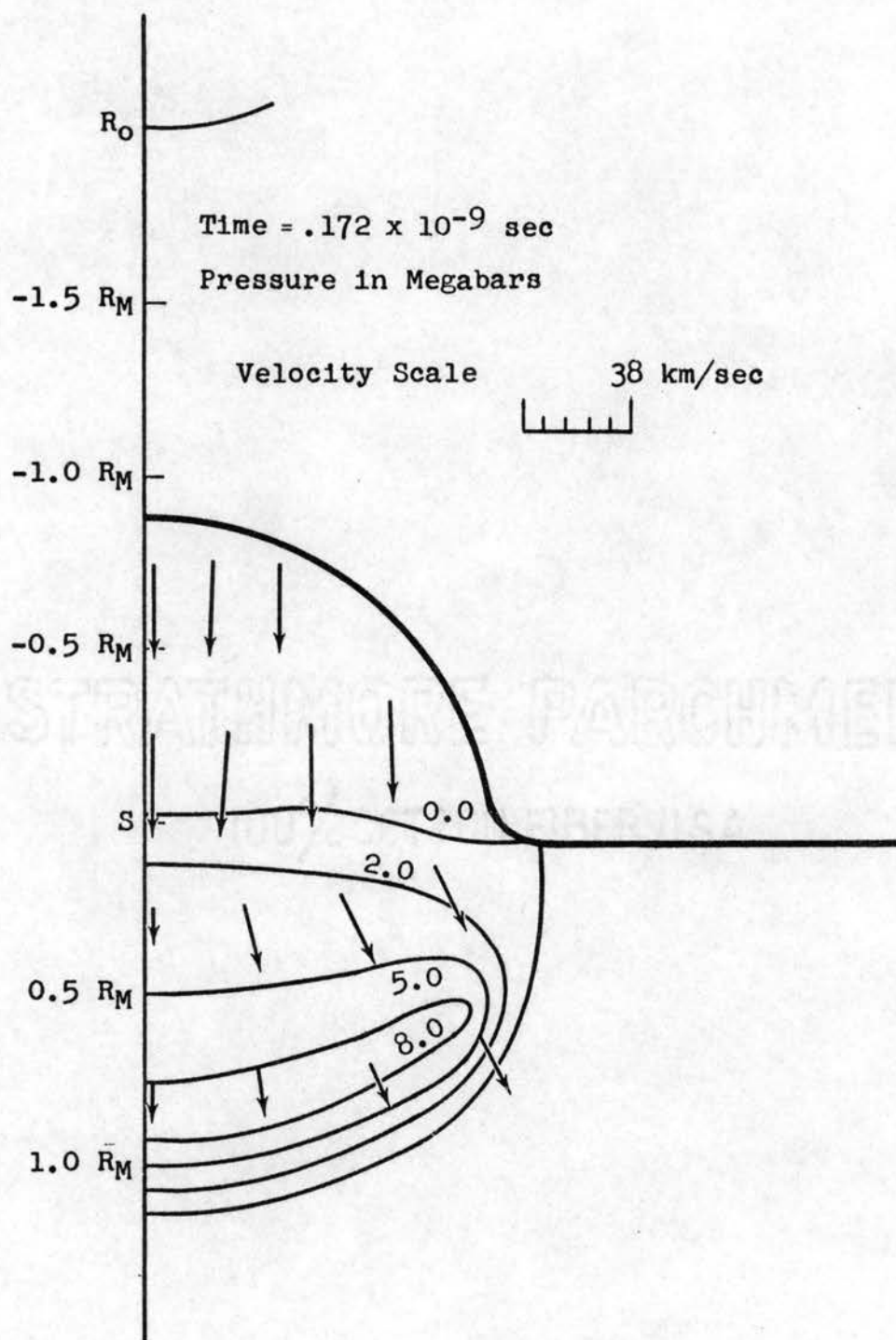


FIGURE 11. PRESSURE CONTOURS AND VELOCITY DISTRIBUTIONS

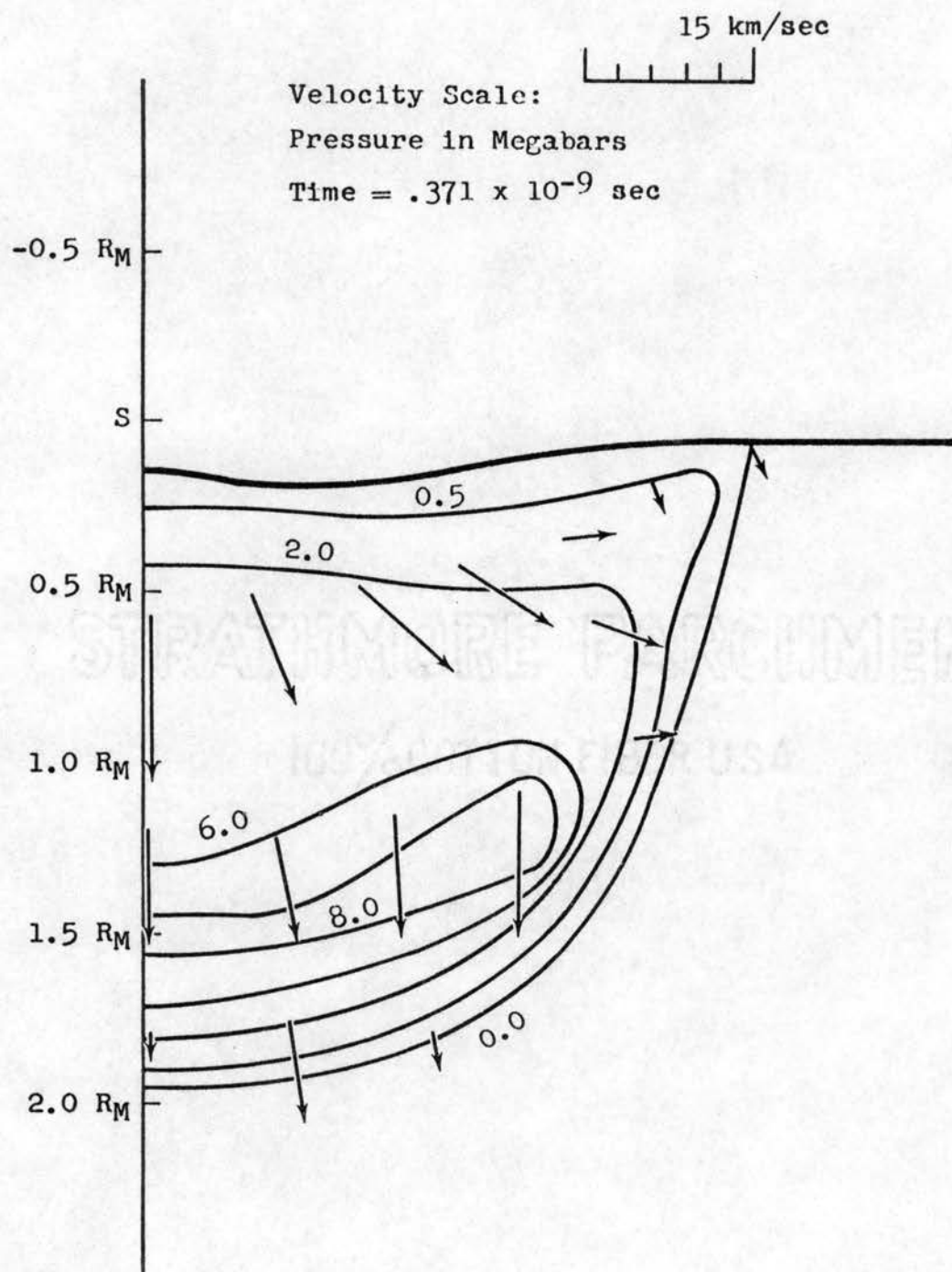


FIGURE 12. PRESSURE CONTOURS AND VELOCITY DISTRIBUTIONS

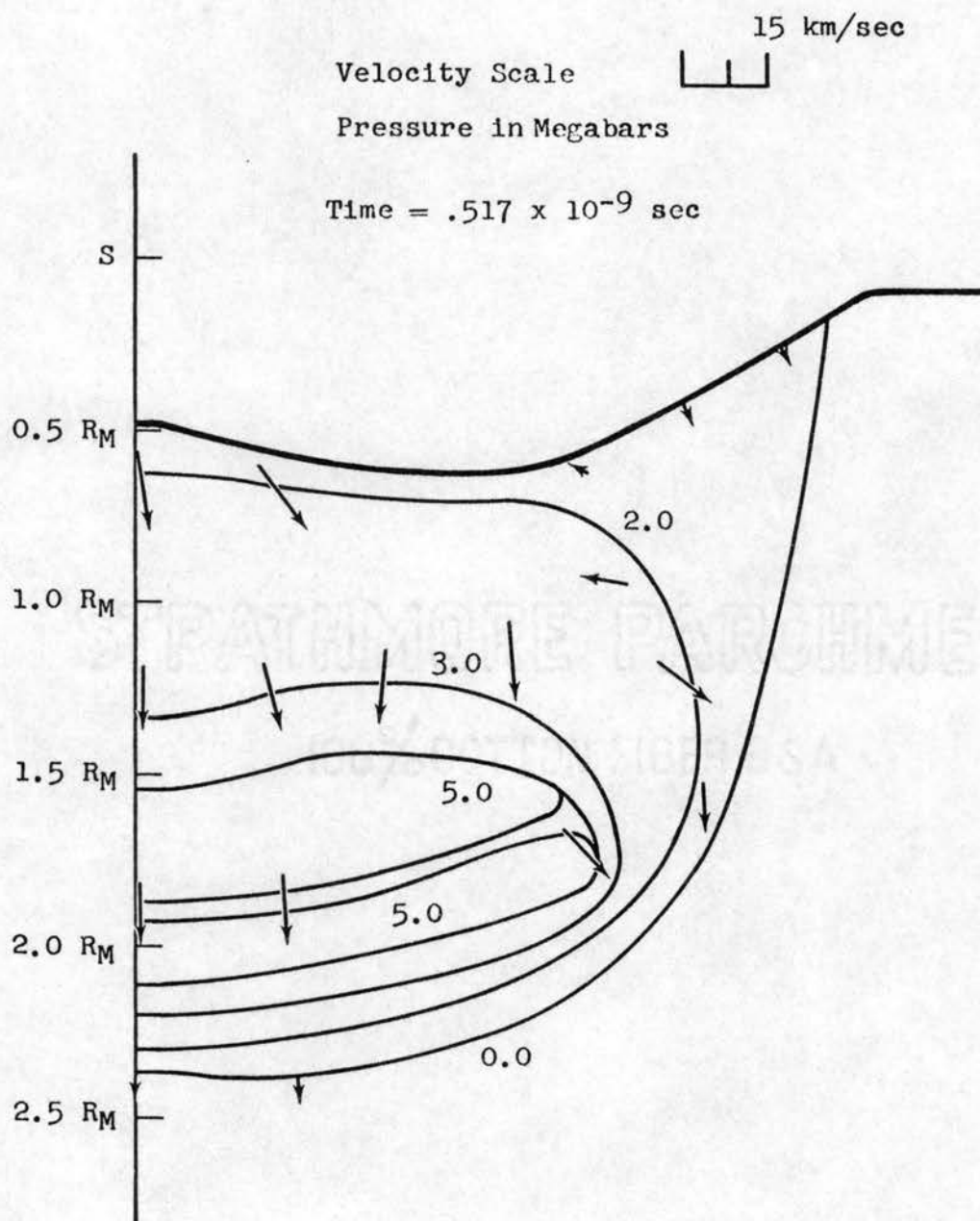


FIGURE 13. PRESSURE CONTOURS AND VELOCITY DISTRIBUTIONS

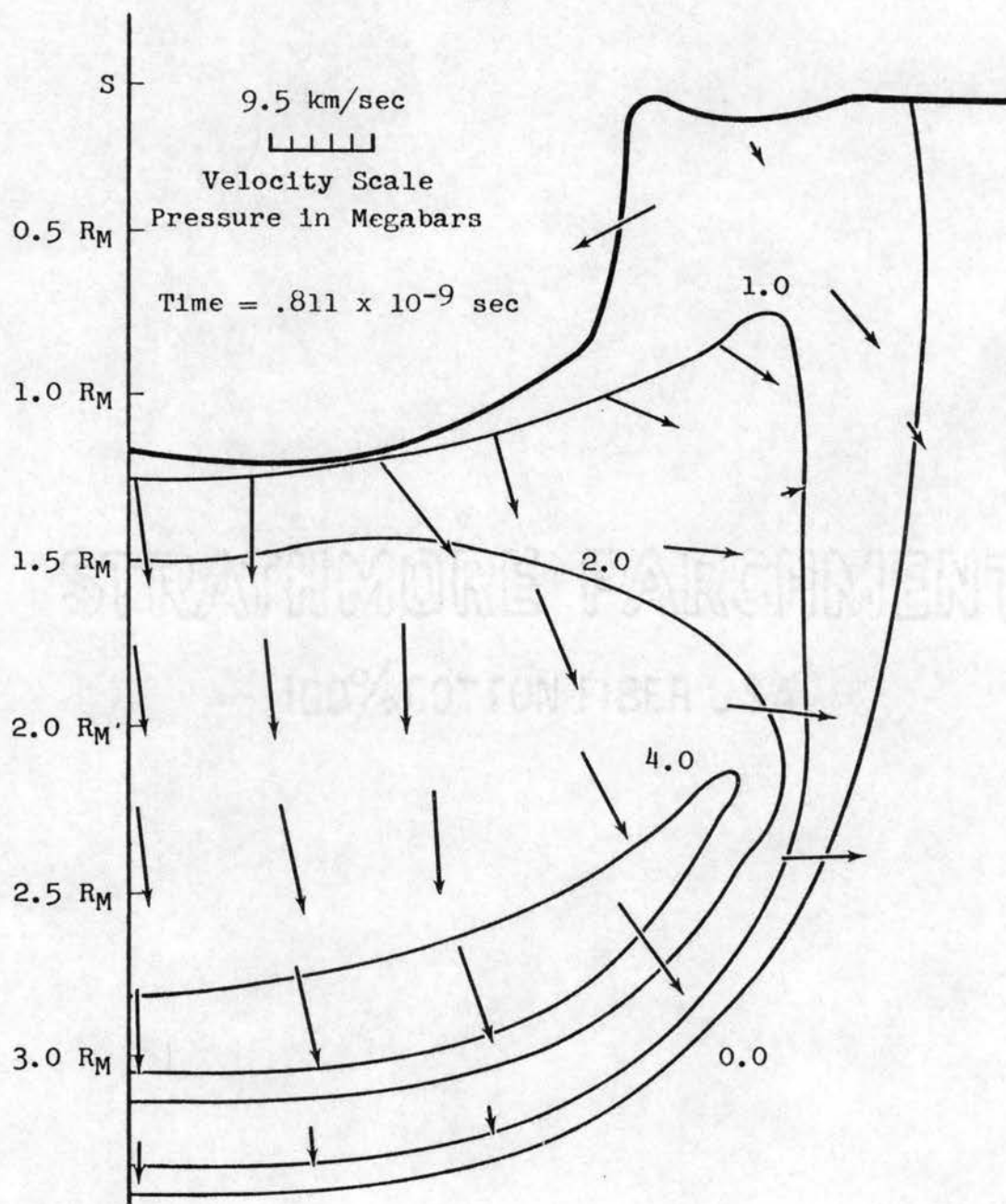


FIGURE 14. PRESSURE CONTOURS AND VELOCITY DISTRIBUTIONS

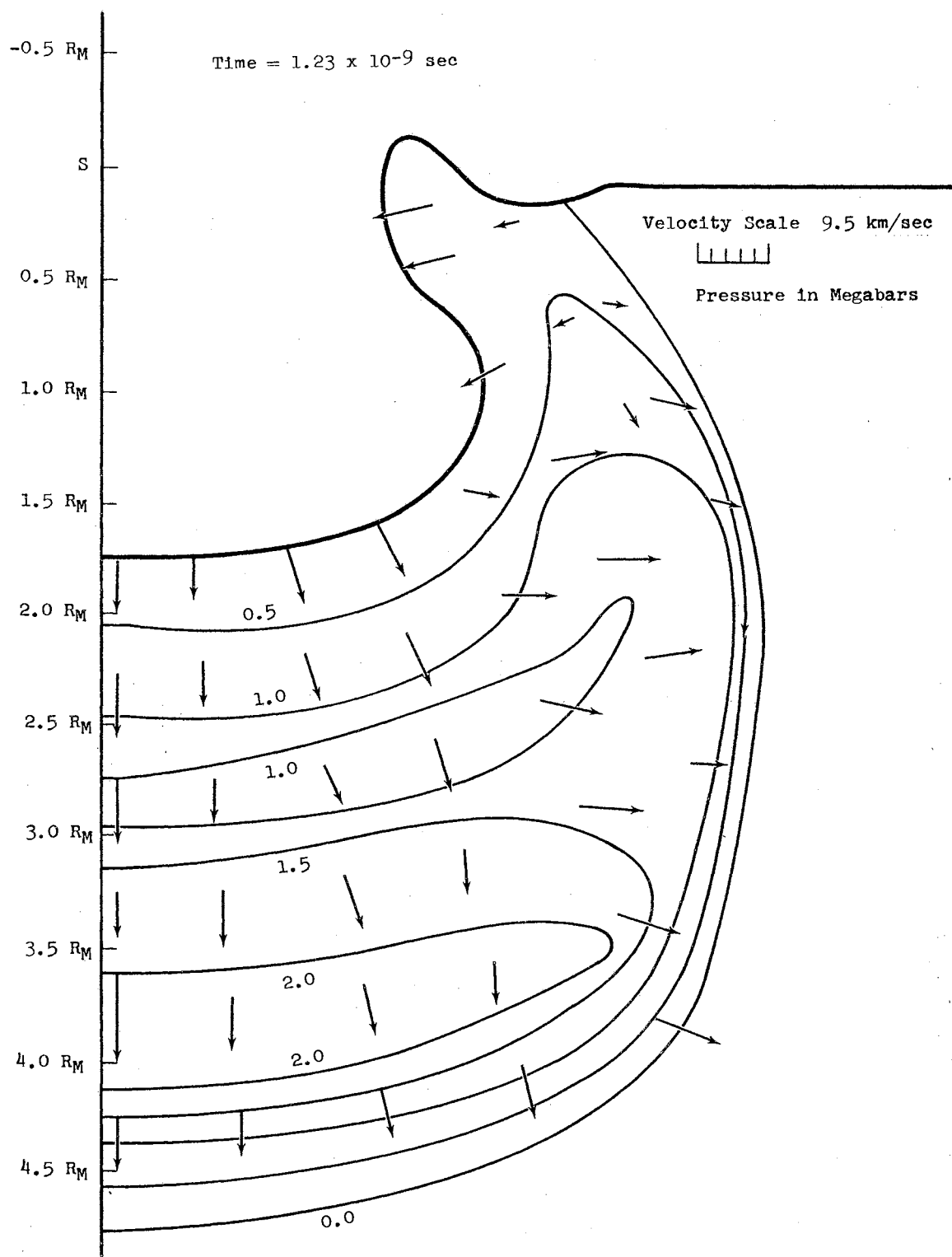


FIGURE 15. PRESSURE CONTOURS AND VELOCITY DISTRIBUTIONS

high velocity while the material of the target is at rest. Some general undulations are seen in the contour maps and may also be discerned by careful inspection of the velocity distributions. This is caused by the particular choice of times and points included in the results and by the nature of numerical solutions.

The velocity distribution in Figure 10-B gives the start of the expansion period of the disturbance. Material moving from the straight line path of the onrushing micro-meteoroid has been put in motion by the primary shock wave rather than by direct contact with the projectile. The maximum pressure developed is twelve megabars. The extent of this peak pressure is shown in Figure 10-B. In an idealized treatment of this impact, the peak pressure would extend to the surface. In the numerical scheme, the motion of fluid particles is communicated from cell to cell in the mesh covering the region of interest. The model chosen probably depicts the physical situation rather well; The peak pressure occurs near the normal axis under the impinging sphere.

The continued growth of the disturbance is shown in Figure 10. The primary shock wave propagates rapidly into the target. This material velocity imparted by the primary front slightly exceeds one-half the original free space velocity of the impinging particle. An impacting

flat plate of aluminum on a semi-infinite slab of aluminum would give exactly one-half the velocity. (23). Further illustrations of full two dimensional material velocity vectors depicting the gross motions to target and sphere will be presented and discussed.

The behavior of the material velocity is unique compared to the other fluid model parameters. At the start of the calculations, all aluminum material is in its normal undisturbed state. The micrometeoroid has initially a very large material velocity which represents the free space velocity of the particle. This leads to the distinctive velocity distributions at initial stages of the impact.

At slightly later times, as shown in Figure 12, the radial character of the fluid disturbance can be seen. The material of the target has a strong tendency to expand away from the regions of direct impact with a material velocity of magnitude approximately one-half the free space velocity of the micrometeoroid. The shape of the disturbed portion of the target material, and the micrometeoroid, can be seen from the pressure distribution in Figure 12. It is near this time that free surface effects begin to influence the solution.

In time, the shock wave traveling to the rear of the micrometeoroid reaches the back edge. It is reflected as a rarefaction wave. The modification of the primary shock wave caused by material expansion is shown in Figure 13.

If the target and projectile had been of different media this first reflection could result in a tension wave proceeding from the free surface. Since the impact process started with aluminum on aluminum, no negative pressures occur.

In one of the later time plots, Figure 14, the radial character of the cavity and disturbance is evident. This shape is a result of the geometry of the impinging micro-particle. Upward motion near the target surface can be seen in Figure 14.

Further propagation of the shock wave provides an illustration of the decay of the primary shock wave as amounts of previously undisturbed aluminum are engulfed. Ultimately, this shock front will reduce to a sound wave of vanishingly small amplitude. The hydrodynamic model does not apply to such late stages of the impact and the solution must be terminated before material properties such as yield strength play an important role. The last results obtained in the computer program are presented in Figure 15. The two distributions are terminal only in an arbitrary sense. They do not and cannot, represent the final stages of crater formation. The deepest part of the cavity is centered about the impact point.

The density behavior of the fluid model is closely related to the pressure of the fluid. Plots of constant density lines for various times will be discussed in the

next section.

Density Distributions

A slightly different view of the impact is given by a series of graphs of constant density contours. These illustrations were drawn in the same manner as the pressure distributions. Constant density contours are shown in Figures 16, 17, and 18. The density value is given as the ratio of material density at a point to that of normal aluminum. Lines marked 1.0 indicate a return to normal conditions.

Density values result from solutions of the continuity of mass equation. Such values together with the internal energy determine the pressure in the hydrodynamic model. At peak pressure and peak density points, however, a shock process is occurring and the equation of state applicable is the Hugoniot curve. Such a relation is apparent at early times in the numerical solution where all disturbances are essentially by shock compression.

In the first stages of micrometeoroid penetration, the density behaves much like the pressure. A peak is formed slightly below the original point of contact. This peak is then broadened into two approximately equal shock waves. The propagation and reflection of these two fronts proceeds as discussed previously. Illustrations of the density variation are found in Figure 16.

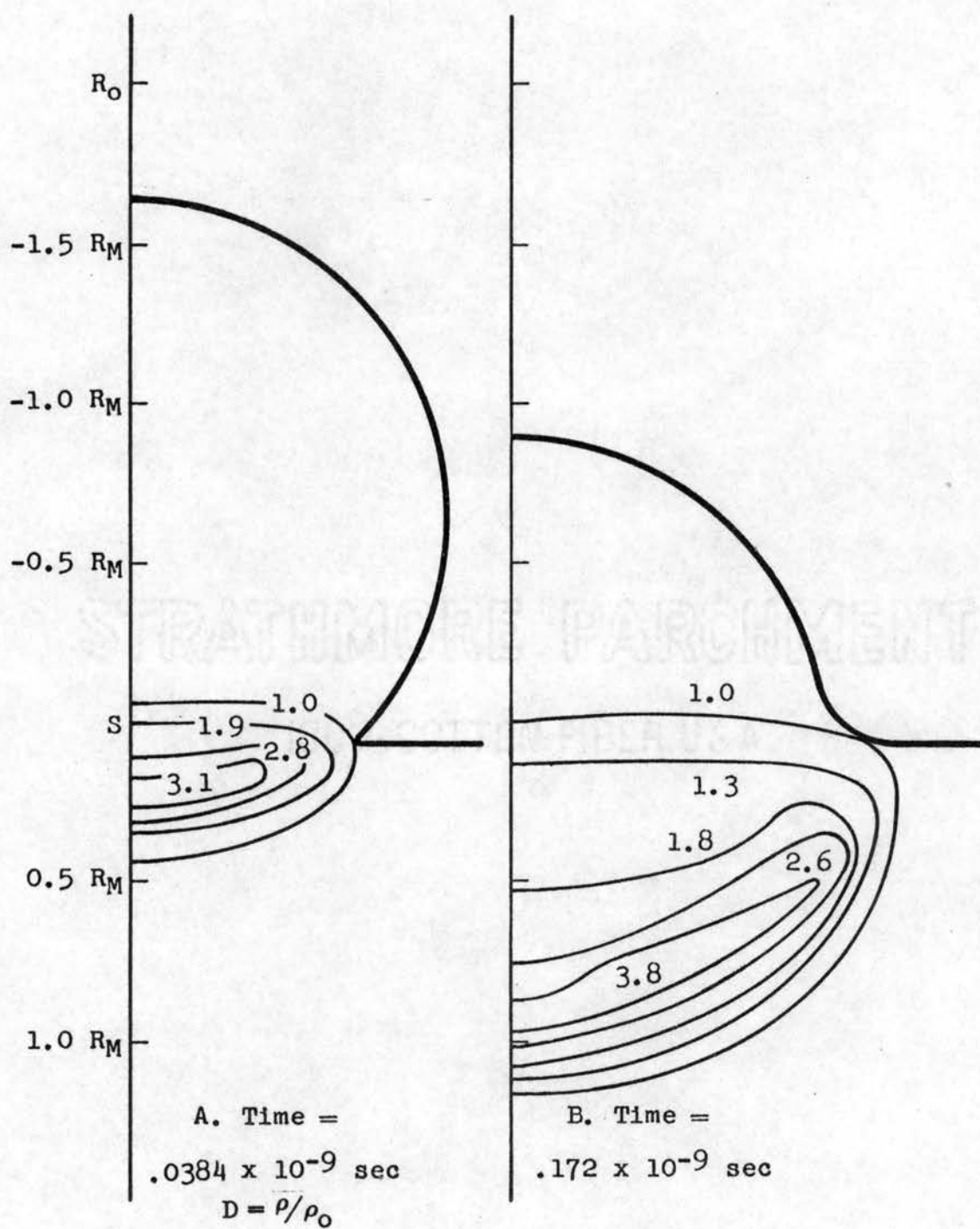


FIGURE 16. CONSTANT DENSITY CONTOURS

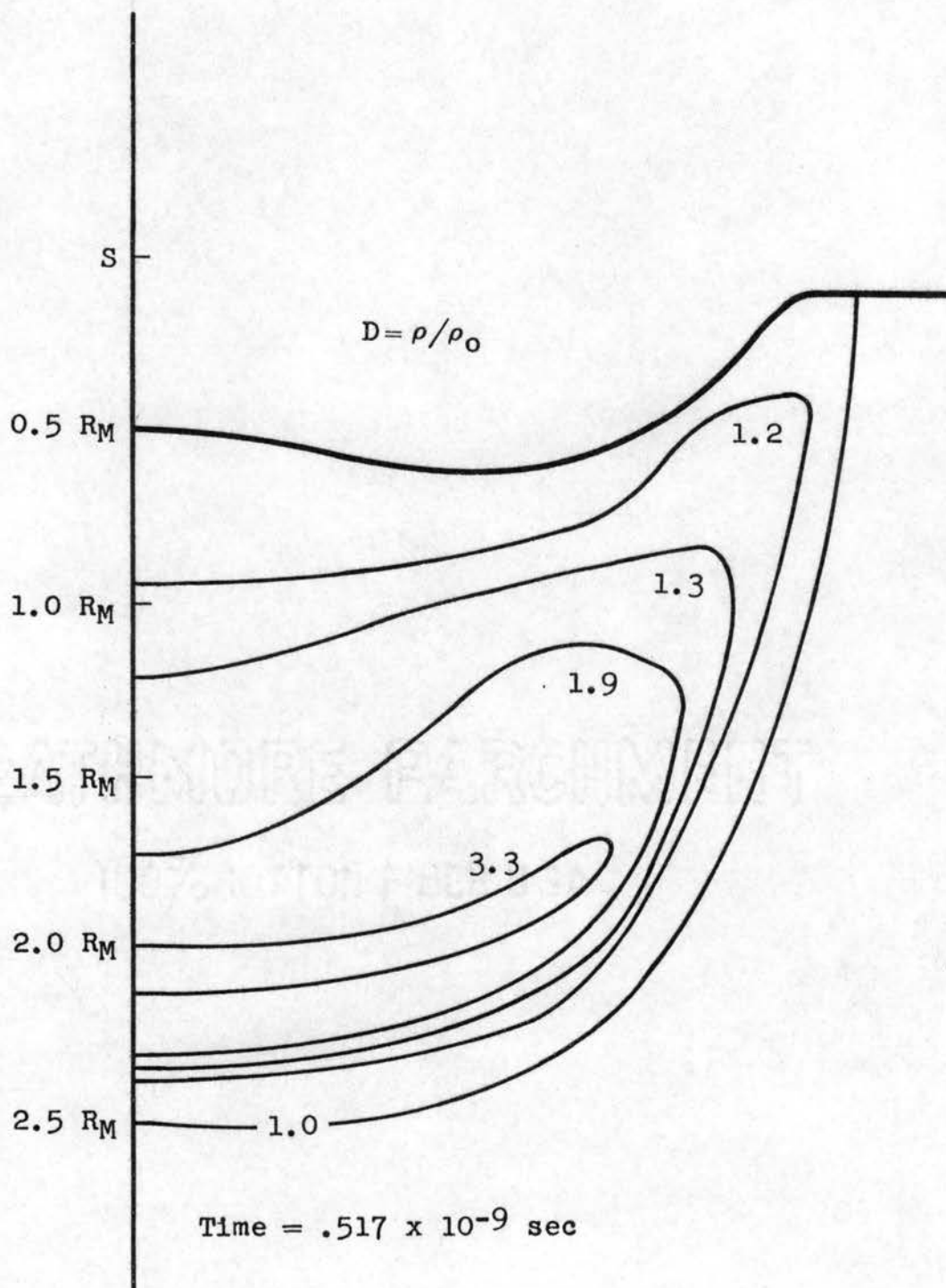


FIGURE 17. CONSTANT DENSITY CONTOURS

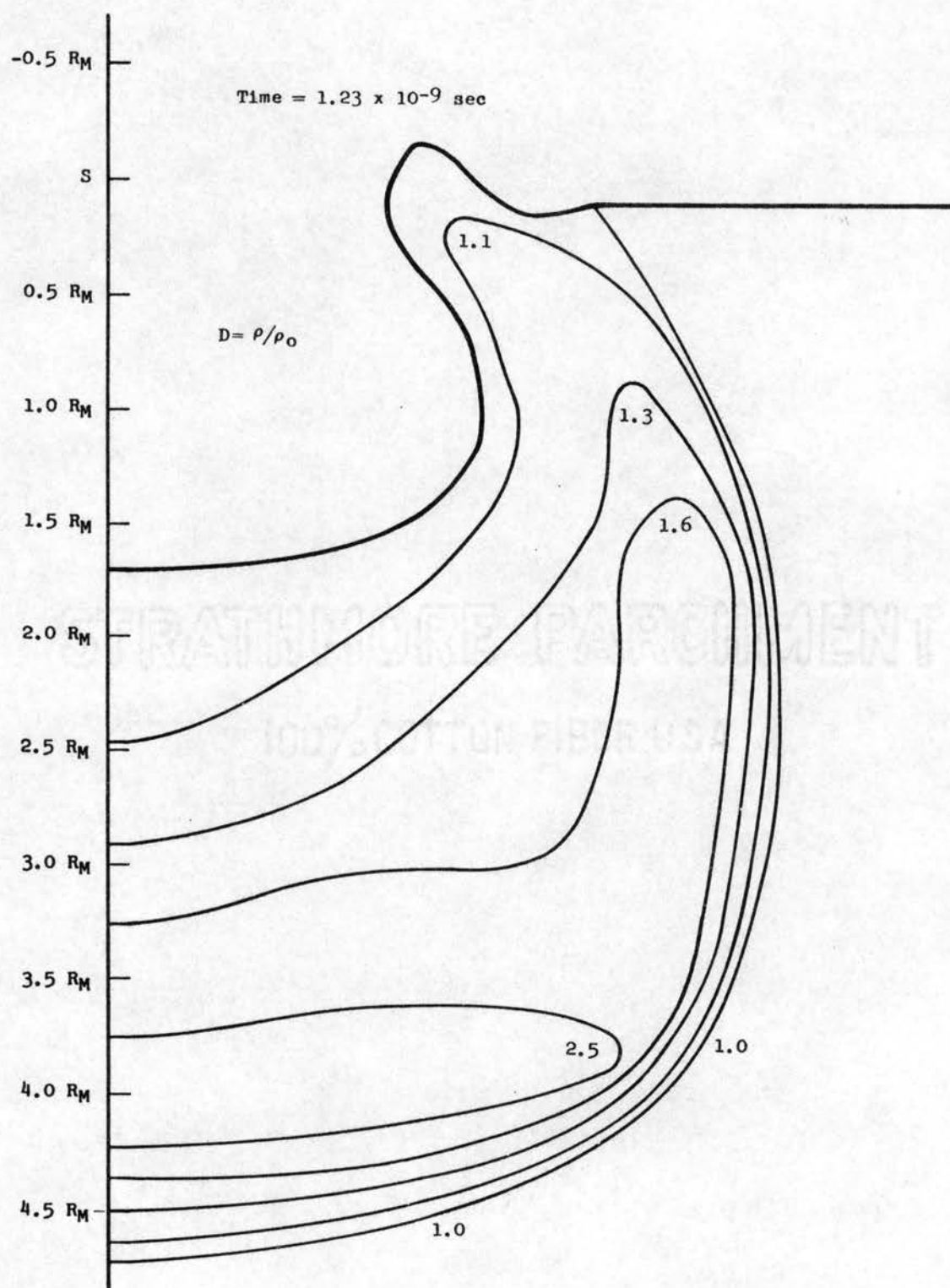


FIGURE 18. CONSTANT DENSITY CONTOURS

Further results of the numerical solutions are given in Figure 17. The dissipation, as with the pressure, is due to rarefaction waves and the ever-increasing volume of action.

Material is seen above the target surface in Figure 18. It is at this time that the condition requiring the density ratio to be equal to or greater than one is first invoked. Material which leaves the target is probably in the form of a fine spray. The average density of this spray, composed of some material clusters and some vacuum between, is undoubtedly less than that of normal aluminum. In failing to adequately describe such states, which would have a negative pressure, the equation of state prevents some motion of the shock wave in the direction perpendicular to the axis of impact.

Internal Energy Distributions

The internal energy is calculated from the total energy which is conserved in the solution of the problem. Contours of constant internal energy are shown in three Figures, 19, 20, and 21. The values of internal energy are given in terms of a reference energy which equals 4.4×10^{12} ergs/gm. The three maps shown are called illustrative rather than exhaustive.

The energy distribution shown in Figure 19 is very similar in shape to the pressure contours at the same time.

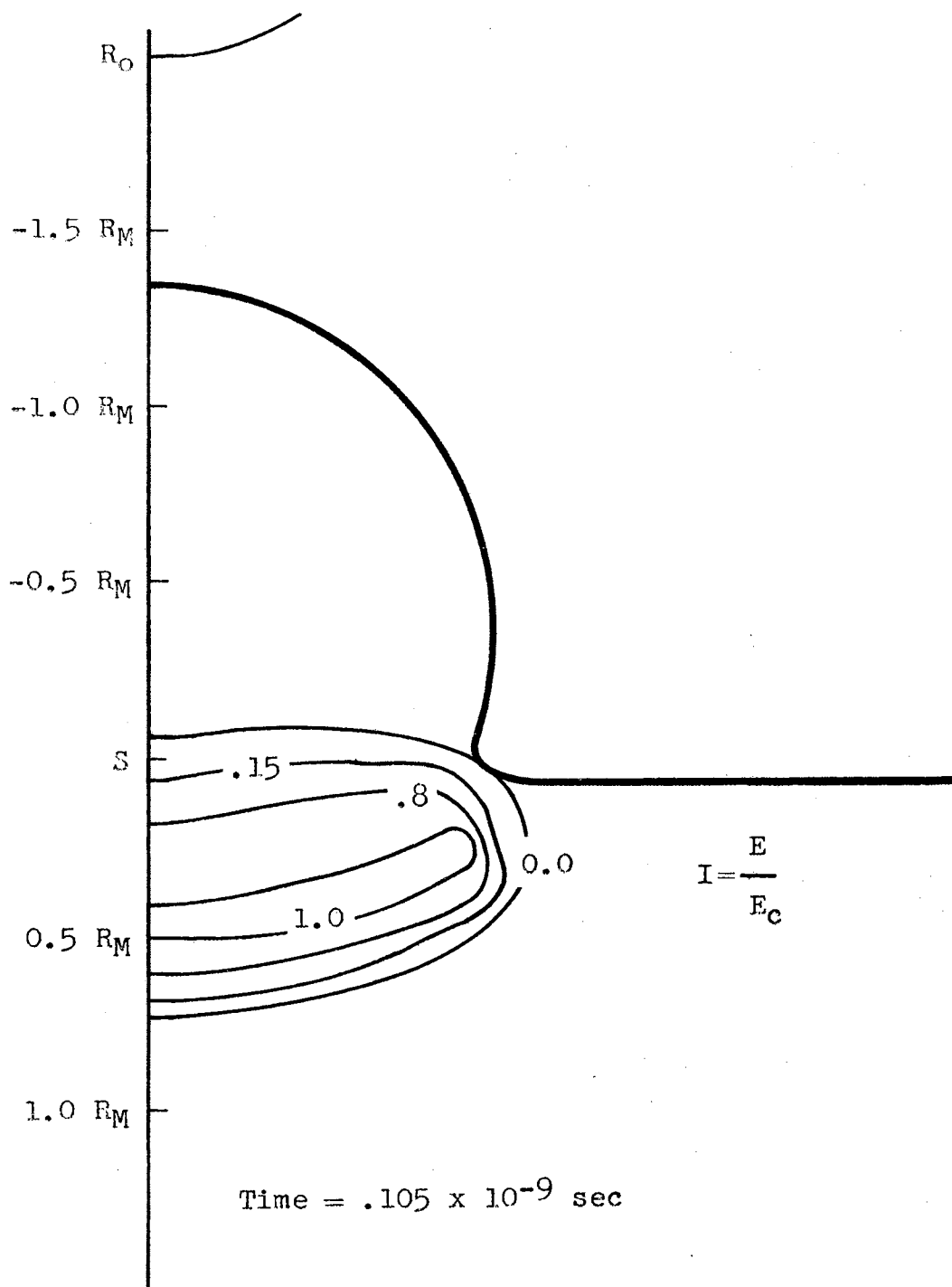


FIGURE 19. CONSTANT ENERGY CONTOURS

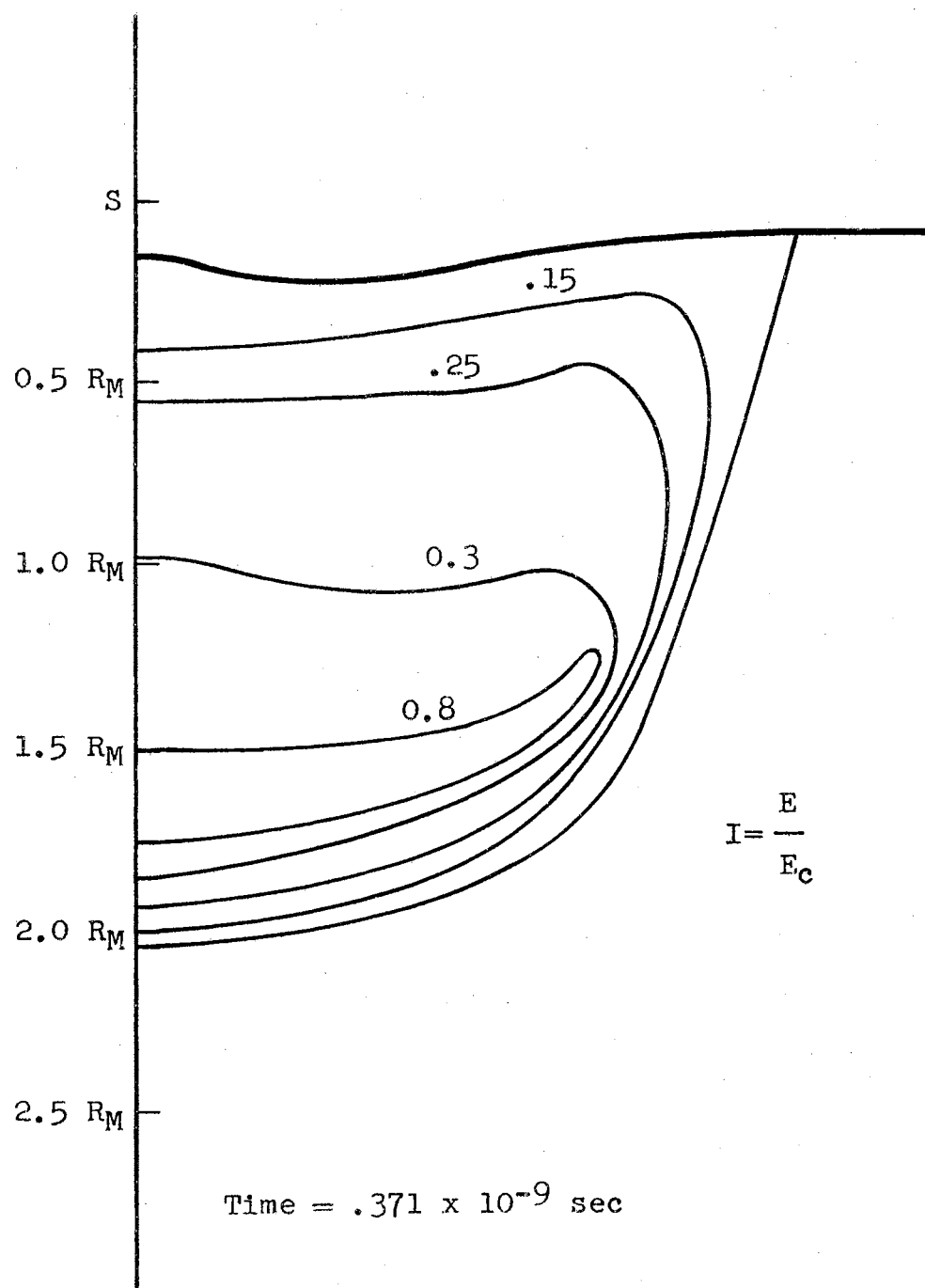


FIGURE 20. CONSTANT ENERGY CONTOURS

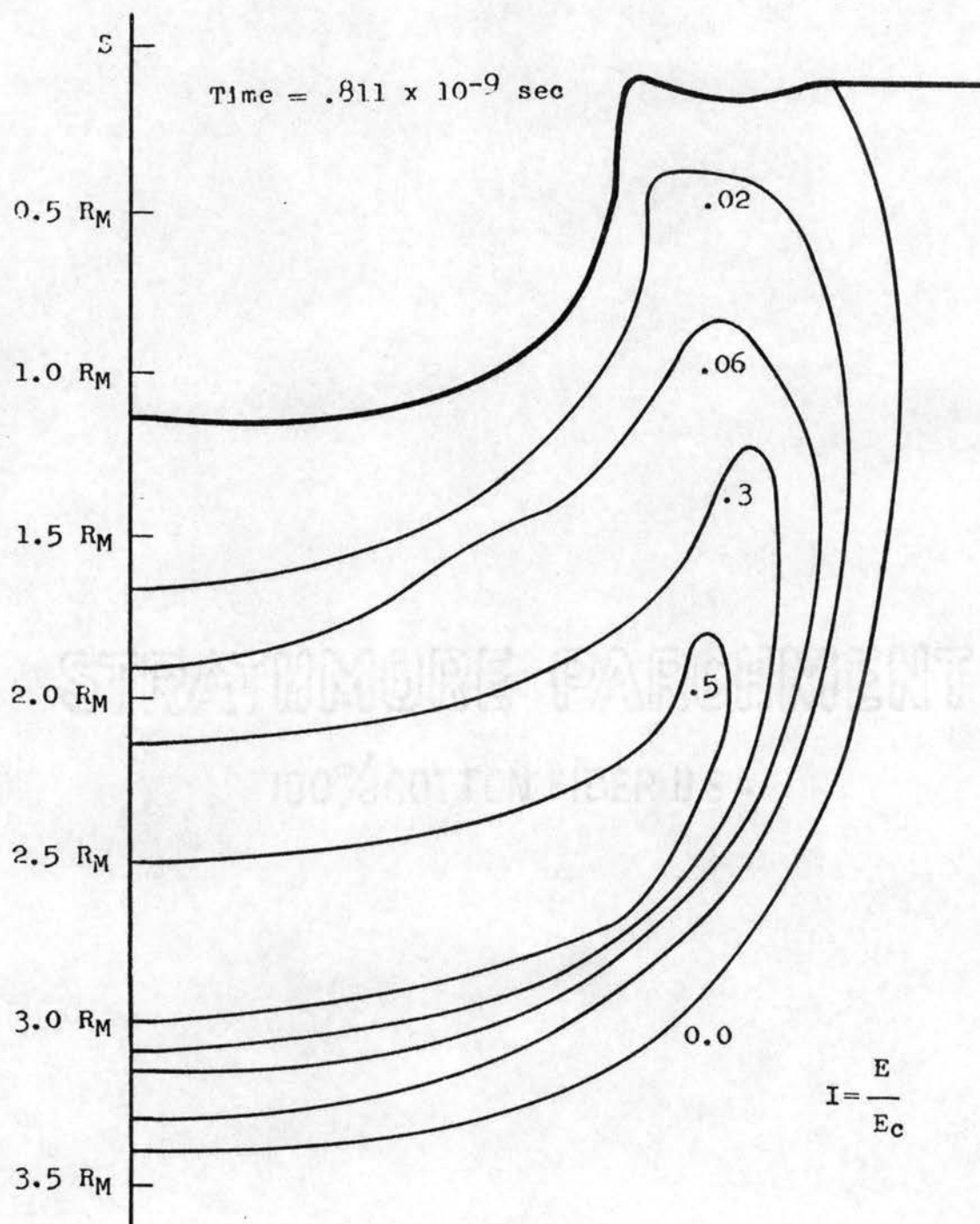


FIGURE 21. CONSTANT ENERGY CONTOURS

There is some slight sluggishness evident in this Figure and in Figure 20. That is, the internal energy does not propagate as rapidly as other fluid parameters.

The shape of the free surface in Figure 21 shows the approximate radial character of the disturbance at this time. The decay, as in other variables is, of course, evident in the values of the constant internal energy lines.

Cavity Formation

The purpose of the study of hypervelocity impact studies is to predict micrometeoroid damage to space vehicles. The assessment of such impacts is quite often done in terms of penetration or crater size related to initial impact velocity values. The numerical solution presented for the hydrodynamic model shows the initial and middle stages of cavity development.

In order to observe the formation of the depression, a series of penetration versus time curves are shown in Figures 22 and 23. Such illustration also give an overall view of the nature of the solution obtained.

The mean velocity of free space micrometeoroids in the vicinity of the earth is about 36 km/sec. (2). Solutions were obtained for an impact of this velocity. Positions of the material surface are shown for various times in Figures 22 and 23. The times for each curve is given in each Figure.

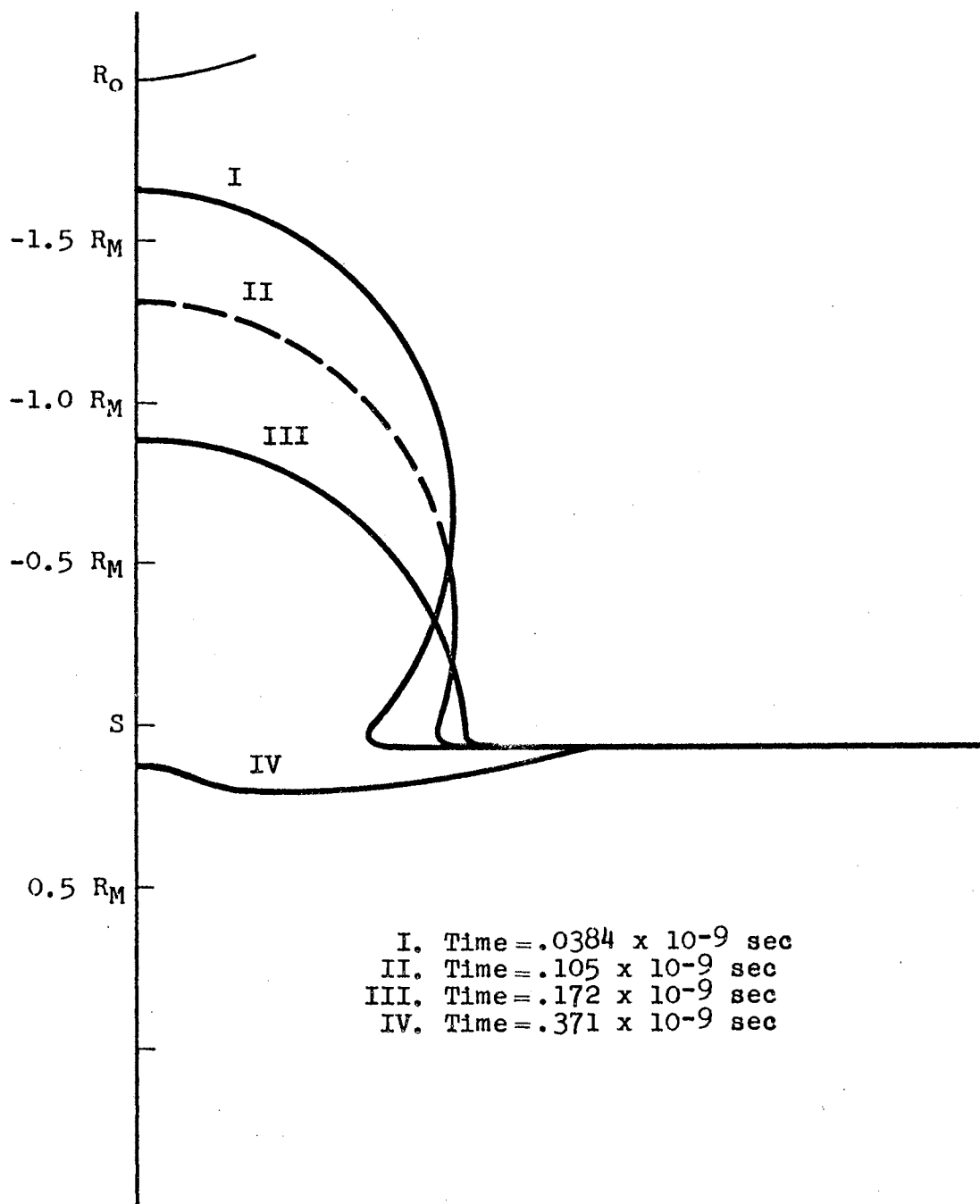


FIGURE 22. POSITION OF SURFACE AT VARIOUS TIMES

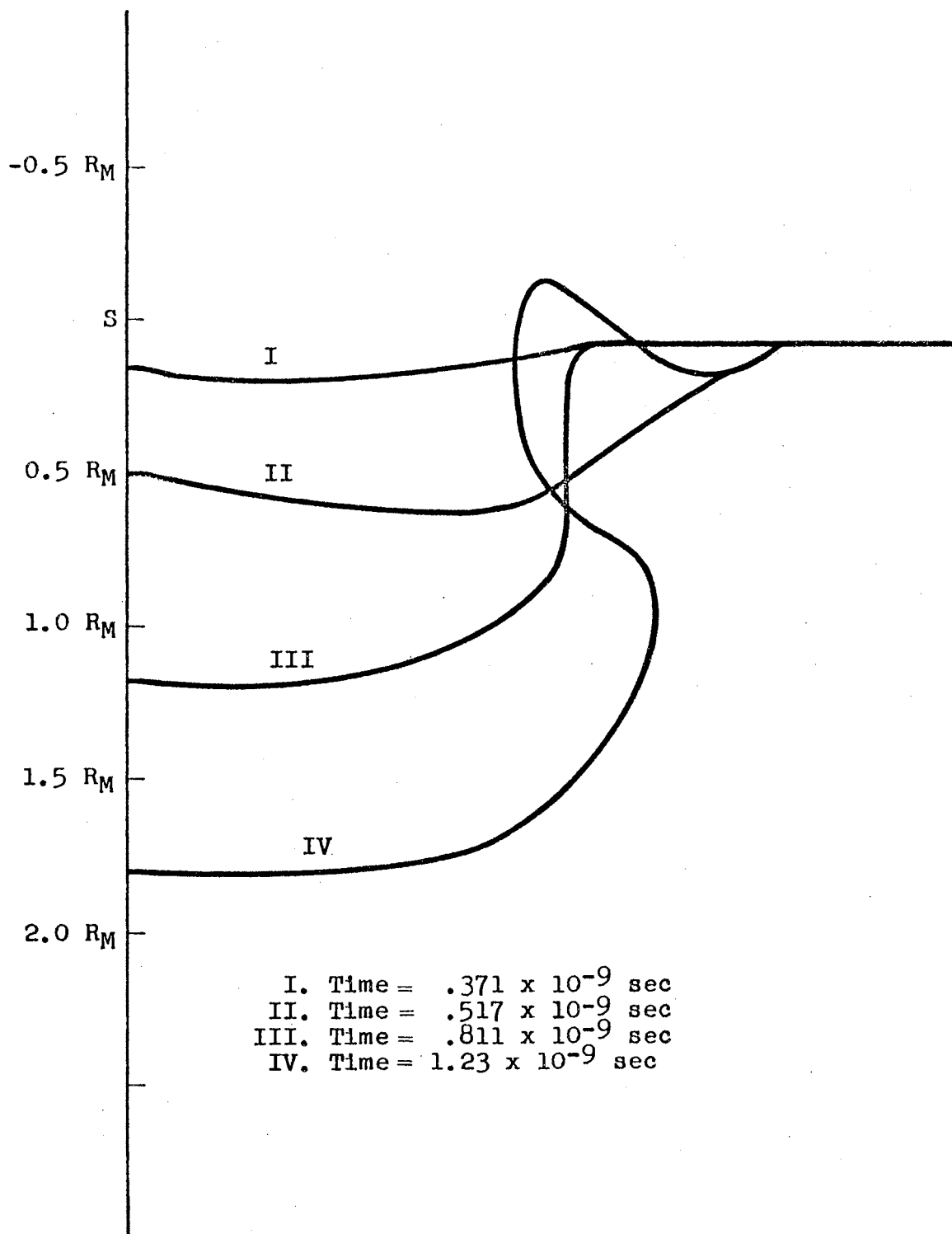


FIGURE 23. POSITION OF SURFACE AT VARIOUS TIMES

The progress of the solution describes the "swallowing" of the incident particle. The momentum and energy transferred from the micrometeoroid to the target compress the aluminum and cause the material to move into the target forming depression.

The initial motions of target and micrometeoroid are followed in Figure 22. At the latest time shown, material from the target is squeezed out by the disturbance of the micrometeoroids entrance. The cavity formation and ejection of material proceed in Figure 23.

The shape of the cavity assumes a radial symmetry about the point of contact. The curves shown bear out this statement, with the deepest portions of the cavity are on a radial arc about S. As seen from the numerical solution there is a strong tendency, evident in the graphs, for some target material to flow away from the entrance path of the micrometeoroid. This activity corresponds to the spray observed in hypervelocity cratering experiments. It is probable that the material expands to such states in which the density is less than that of normal aluminum. The equation of state, however, only allows states of compression or, at least, zero pressure. The density is required to be equal to or greater than normal density. This provision leads to an impasse near the distorted portion of the surface where it is probable that densities less than normal would be seen. The shock wave moving in

the lateral direction cannot propagate as freely as the pressure front penetrating along the normal axis.

Dissipation of the Peak Pressure

A plot of pressure decay has been prepared and is presented in Figure 24. This is shown in order to illustrate the rapid decay of the peak pressure. These peak value dissipation traces also permit correlation with experimental data and other theoretical calculations.

The curves are drawn using the approximate peak pressure along the normal axis versus the position of this function on the normal axis. There is some uncertainty concerning the exact point to point comparison, but the average curves yield a satisfactory indication of the decay rate. Distance along the axis is measured in units of the micrometeoroid radius, R_M , from the point of impact, S. As R increases, there is some uncertainty in interpreting the peak pressure and the large scale of the drawings seems to indicate a decay to a constant state. This is not observed in the results as can be verified by reference to full pressure distributions.

For the case of an impact velocity of 36 km/sec., sufficient information was obtained from the numerical solution to indicate the growth to a peak pressure of 12 megabars and the subsequent decay. This value is found

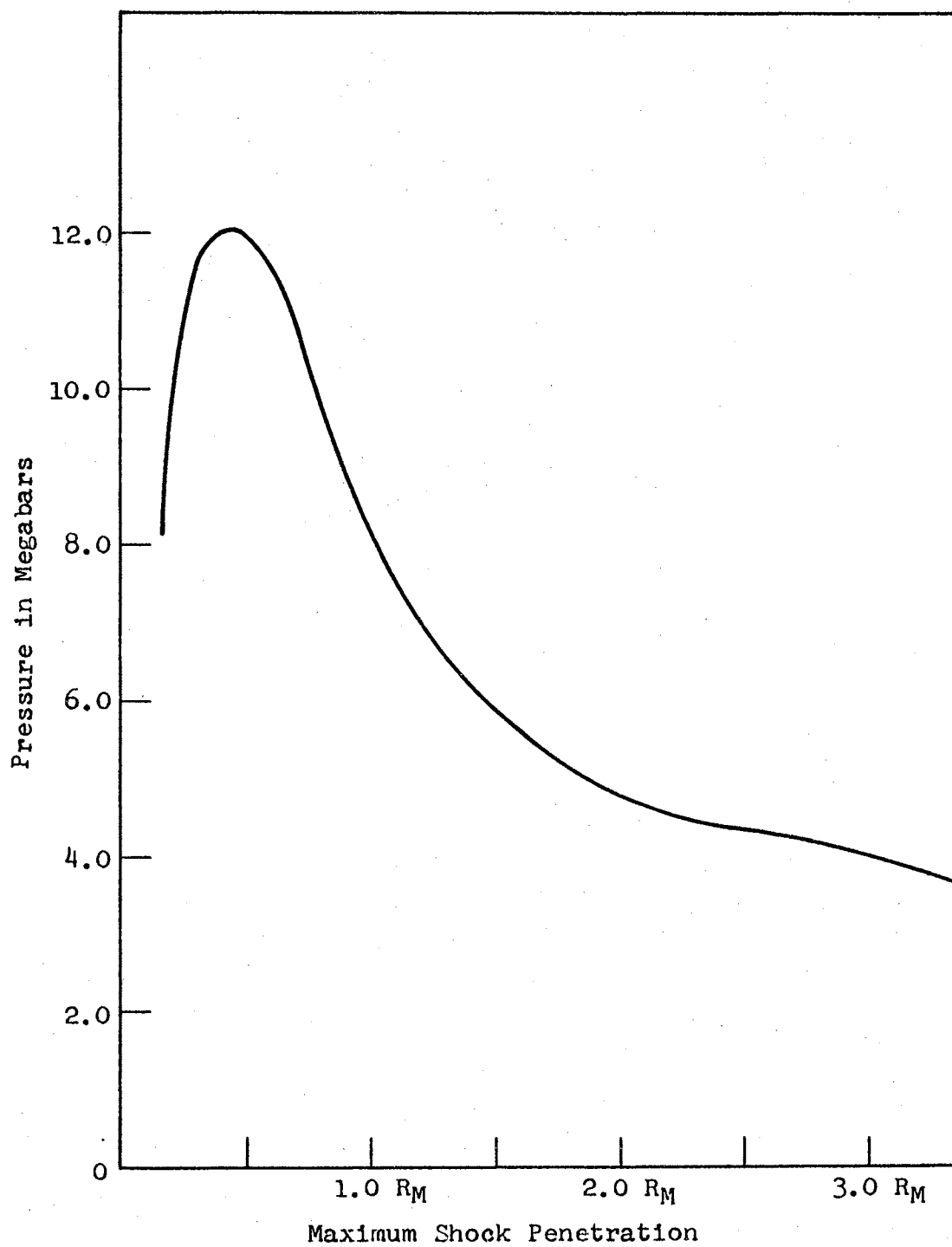


FIGURE 24. PEAK SHOCK PRESSURE AS A FUNCTION OF MAXIMUM SHOCK PENETRATION

in other shock propagation calculations (4, 14).

Such a curve gives an indication of the transient nature of the peak pressure which occurs in an impact process. This peak pressure, however, determines the subsequent states of the affected target material and perhaps ultimately the crater size and terminal mechanisms.

Discussion of Results

The most interesting feature of this data is the production of two distinct shock waves at the point of initial contact. Both shock waves are of approximately equal strength traveling in opposite directions. There is some asymmetry in the forward direction, however; the primary shock front is somewhat stronger since it moves into undisturbed material. The progress of such waves is followed until free boundary reflection of one wave and considerable decay of the primary shock front modify the flow patterns. The start and growth of the cratering process have been fully depicted. A complete description must be found in other material regimes, such as the plastic and elastic. The radial character of the cavity becomes apparent at later times when material begins to flow out of the target.

CHAPTER V

SUMMARY AND SUGGESTIONS FOR FUTURE WORK

Calculations for the impact of a spherical aluminum microparticle on a semi-infinite aluminum target have been presented. A numerical method was developed and tested for the solution of a set of Eulerian, dimensionless, equations. These equations include shock wave propagation and target motion. A FORTRAN IV computer program has been used to obtain solutions for all cases up to a time when the decay of the primary shock front is significant.

A basic feature of these solutions is the formation of two shock waves at the position of initial contact of microparticle and target. One shock front, the primary shock wave, travels into the target compressing material of the target. The other, moving into the projectile, is reflected at the material-vacuum boundary. The resulting rarefaction wave eventually overtakes the primary wave and weakens it. Another feature noted in the curves depicts the start of a crater and the ejection of material above the original target surface. The impacting microparticle appears to compress the target material ahead of and surrounding

itself. This results in the flow of the target material up, around the entering particle and out of the target.

As the disturbance engulfs more target material, the hydrodynamic pressures become comparable to yield stresses. It is then inappropriate to neglect material strength and the hydrodynamic model becomes inapplicable. This same difficulty occurs earlier near the free surfaces involved in the problem. Consideration of necessary descriptive equations of the plastic and elastic states in addition to the hydrodynamic state will give a more complete description of micrometeoroid impact.

It is believed that inclusion of plasma properties in the equation of state, and addition of plasma conservation equations to the modified Eulerian set, would explain the radiation observed in the impact process.

These extensions, the refinement of the hydrodynamic model to include plasma, plastic, and elastic material should lead to a better understanding of the hypervelocity impact problem.

SELECTED BIBLIOGRAPHY

1. Collins, R. D., and W. Kinard. NASA TN D- 230 (May, 1960).
2. Alexander, W. M., O. E. Berg, and M. Dubin. Direct Measurements of Cosmic Dust Showers. NASA TN D-1544 (January, 1963).
3. Cook, M. A. "Mechanism of Cratering in Ultra-High Velocity Impact," J. Appl. Phys. 30 (1959) 725-735.
4. Lake, H. R. "Digital Computer Solution for Propagation of a Spherical Shock Wave in Aluminum," Master's Thesis, Oklahoma State University (1962).
5. Bjork, R. L. "Effects of a Meteoroid Impact on Steel and Aluminum in Space." Engineering Division, RAND Corporation, P-1622 (1958).
6. Todd, F. C. and H. R. Lake. "Analytical and Limited Experimental Study of the Mechanisms of Impact, Penetration and Light Emission for Micrometeorites on an Aluminum-Coated Photomultiplier." Quarterly Progress Report, No. 1. NASr-7, Research Foundation, Oklahoma State University, December 31, 1960.
7. Hamann, S. D. Physico-Chemical Effects of Pressure. New York: Academic Press (1957), 57-60.
8. Charters, A. C. "High Velocity Impact," Scientific American 203 (October, 1960), 128-140.
9. Richtmyer, R. D. Difference Methods of Initial-Value Problems. New York: Interscience Publishers (1957), 207.
10. Von Neumann, J. and R. D. Richtmyer. "A Method for the Numerical Calculations of Hydrodynamic Shocks," J. Appl. Phys. 21 (1950), 232-237.
11. Landshoff, R. A Numerical Method for Treating Fluid Flow in the Presence of Shocks. Los Alamos Report LAMS-2379 (April, 1959).

12. Walsh, J.M., N. H. Rice and R. G. McQueen. "Compression of Solids by Strong Shock Waves," in Solid State Physics, 6, 1-63. New York: Academic Press (1958).
13. Marsh, N. H. "The Thomas-Fermi Approximation in Quantum Mechanics, " Adv. in Phys. 6 (1957), 1-101.
14. Sodek, B. A., Jr. "The Penetration of an Aluminum-Glass Interface by an Originally Radial Shock Wave," Master's thesis, Oklahoma State University (1965).
15. 1. c. 9, p. 199.
16. Tillotson, J. H. Metallic Equations of State for Hypervelocity Impact. General Atomic report GA-3216 (July, 1962).
17. Bjork, R., N. Brooks, and R. Papetti. A Numerical Technique for Solution of Multidimension Hydrodynamic Problems. The RAND Corporation Memorandum RM-2628-PR (December, 1963).
18. 1. c. 9, p. 38.
19. 1. c. 9, p. 40.
20. 1. c. 9. p. 77.
21. 1. c. 9, p. 169.
22. 1. c. 9, p. 197.
23. Sodek, B. A. and F. C. Todd. "Penetration of an Initially Radial Shock Wave Through an Aluminum-Glass Interface," Proc. Okla. Acad. Sci. 43 (1963) 173-182.
24. Rae, W. J. and H. P. Kirchner, "A Blast-Wave Theory of Crater Formation in Semi-Infinite Targets." Proceedings of the Sixth Symposium on Hypervelocity Impact, 1962, Vol. II, Part 1, pp. 163-227.

VITA

Benard A. Sodek, Jr.

Candidate for the Degree of

Doctor of Philosophy

Thesis: A HYDRODYNAMIC MODEL OF MICROMETEOROID IMPACT

Major Field: Physics

Biographical:

Personal Data: Born in Dallas, Texas, January 22, 1937, the son of Benard A. and Victoria Ruth Sodek. Married N. Gail Swords in May, 1959. Father of three children: Lorriedel, Benard III, and Alexander.

Education: Graduated from Sacred Heart Cathedral Grammar School, Dallas, Texas, in May, 1951. Awarded scholastic scholarship for four years at Jesuit High School, Dallas, Texas. Graduated as Valedictorian in May, 1955. Awarded scholastic scholarship for two years at the Loyola University of the South, New Orleans, Louisiana. Graduated with a Bachelor of Science degree in May, 1959. Received the Master of Science degree from Oklahoma State University in May, 1965. Completed requirements for the degree of Doctor of Philosophy in physics from Oklahoma State University, Stillwater, Oklahoma, in May, 1966.

Professional Experience and Organizations: Presently Research Scientist in Applied Research Group of General Dynamics, Ft. Worth; Graduate assistant in Department of Physics, Oklahoma State University, 1959-1960; research assistant, 1960-1964. Member of Sigma Pi Sigma, Oklahoma Academy of Science, and the American Physical Society.